



Original Paper

Enlightenment of geochemistry for ultra-deep petroleum accumulation: Coupling of secondary processes and filling events

Rong-Zhen Qiao ^{a, b, c}, Mei-Jun Li ^{a, b, c, *}, Dong-Lin Zhang ^{a, b, c}, Hong Xiao ^{a, b, c}^a Hainan Institute of China University of Petroleum (Beijing), Sanya, 572025, Hainan, China^b State Key Laboratory of Petroleum Resources and Engineering, Beijing, 102249, China^c College of Geosciences, China University of Petroleum (Beijing), Beijing, 102249, China

ARTICLE INFO

Article history:

Received 23 March 2024

Received in revised form

18 October 2024

Accepted 25 February 2025

Available online 27 February 2025

Edited by Jie Hao

Keywords:

Ultra-deep

Geochemistry

Secondary processes

Igneous intrusions

Petroleum accumulation

ABSTRACT

Light oil and gas reservoirs are abundant in the Ordovician marine carbonate reservoir in Shunbei Oil-field, Tarim Basin. This presents a compelling geological puzzle, as ultra-deep reservoirs undergo intense alteration and complex petroleum accumulation processes. A comprehensive suite of geochemical analyses, including molecular components, carbon isotope composition, homogenization temperature of saline inclusions, and burial-thermal history of single wells, was conducted to elucidate the genesis of these ancient reservoirs. Three petroleum filling events have been identified in the study area: Late Caledonian, Hercynian-Indosinian, and Himalayan, through analysis of homogenization temperatures of brine inclusions and burial-thermal histories. Additionally, the oil in the study area has undergone significant alteration processes such as biodegradation, thermal alteration, mixing, evaporative fractionation, and gas invasion. This study particularly emphasizes the influential role of Himalayan gas filling-induced evaporation fractionation and gas invasion in shaping the present petroleum phase distribution. Furthermore, analysis of light hydrocarbon and diamondoid parameters indicates the oil within the study area is at a high maturity stage, with equivalent vitrinite reflectance values ranging from 1.48% to 1.99%. Additionally, the analysis of light hydrocarbons, aromatics, and thiadiamondoids indicates that TSR should occur in reservoirs near the gypsum-salt layers in the Cambrian. The existence of the Cambrian petroleum system in the study area is strongly confirmed when considering the analysis results of natural gas type (oil cracking gas), evaporative fractionation, and gas invasion. Permian local thermal anomalies notably emerge as a significant factor contributing to the destruction of biomarkers in oil. For oil not subject to transient, abnormal thermal events, biomarker reliability extends to at least 190 °C. In conclusion, examining the special formation mechanisms and conditions of various secondary processes can offer valuable insights for reconstructing the history of petroleum accumulation in ultra-deep reservoirs. This research provides a scientific foundation for advancing our knowledge of petroleum systems and underscores the importance of hydrocarbon geochemistry in unraveling ultra-deep, complex geological phenomena.

© 2025 The Authors. Publishing services by Elsevier B.V. on behalf of KeAi Communications Co. Ltd. This is an open access article under the CC BY-NC-ND license (<http://creativecommons.org/licenses/by-nc-nd/4.0/>).

1. Introduction

Advances in drilling technology have driven global petroleum exploration towards ultra-deep regions, defined as reservoir depths exceeding 6000 m. A pivotal milestone was the drilling of the Kola 3 well in the former Soviet Union in the 1970s. It reached a remarkable vertical depth of 12,262 m, earning the distinction of being the

world's first 10,000-m-deep well (He et al., 2023). Subsequent decades witnessed a surge in ultra-deep drilling. At present, sixty-seven wells with drilling depths exceeding 10,000 m are predominantly clustered in oil-rich nations such as Russia, the United States, Mexico, and the United Arab Emirates (Yao et al., 2018). In addition to energy exploration, ultra-deep scientific drilling offers a unique "window" for studying fluid dynamics, geothermal energy, and seismic activity in the deep Earth.

China's ultra-deep petroleum resources are abundant and highly prospective. These resources constitute approximately 34%

* Corresponding author.

E-mail address: meijunli@cup.edu.cn (M.-J. Li).

of China's total petroleum reserves. At present, China's ultra-deep petroleum resources primarily exist in carbonate reservoirs in superimposed basins across central and western China, including the Ordos Basin, Sichuan Basin, and Tarim Basin (Du et al., 2019; Fang et al., 2024). Notably, the Tarim Basin has emerged as a focal point. At present, several ultra-deep oil fields have been discovered, including the Tahe, Halahatang, Lungu, Tazhong, Hudson, Fuman, and Shunbei fields (Zhu et al., 2019; Wang et al., 2021, 2023; Qi et al., 2022; Zhang et al., 2022). Additionally, ZS1C well extracts industrial petroleum from Cambrian carbonate reservoirs rich in evaporites such as gypsum (Zhu et al., 2019). The TS5 well yielded liquid hydrocarbons in the dolomite reservoir of the Sinian Qigebulake Formation (Z_{2q}) at 9017 m (Cao et al., 2024). The existence of effective pre-Cambrian source rocks has previously been met with skepticism due to limitations in exploration and drilling technologies (Kontorovich et al., 2005). Nevertheless, recent breakthroughs in petroleum exploration have significantly affirmed the exploration potential of ancient sedimentary reservoirs (Ordovician, Cambrian, and pre-Cambrian). Simultaneously, it suggests the presence of more abundant organic organisms in the Precambrian, which had conditions conducive to well-developed source rocks.

The Shunbei Oilfield is situated in the heart of the Taklimakan Desert. In 2015, the SHB1-1H well in the No. 1 fault zone (F1) produced significant industrial oil, marking the beginning of another Palaeozoic marine oilfield with reserves of 100 million tons in the Tarim Basin. Subsequently, abundant petroleum discoveries were made in the Ordovician reservoirs (O_{2yj} and O_{1-2y}) across fault zones F1, F2, F4, F5, F6, F7, F8, F10, F12, and F14 (Zhu et al., 2019; Chen et al., 2021; Wang et al., 2021; Ma et al., 2022; Zhang et al., 2024). Regional petroleum properties exhibit significant variations, displaying a distinct distribution pattern known as "south gas and north oil" (Chen et al., 2021). Previous studies primarily focused on the geochemical characteristics and petroleum filling events of fault zones F1, F2, F4, and F5 (Chen et al., 2021; Wang et al., 2021). However, the geochemical characteristics and petroleum filling events of fault zones F6, F8, F10, and F12 remain unexplored. Additionally, previous studies focused mainly on individual fault zones, resulting in limited geochemical data from oil samples and hindering a comprehensive evaluation of chemical characteristics across the entire Shunbei Oilfield. Thus, a comprehensive analysis is necessary to elucidate the geochemical characteristics across the entirety of the Shunbei Oilfield.

The study analyzed core, oil, and gas samples from fault zones F6, F8, F10, F12, and F14 in the Shunbei Oilfield. Primary target reservoirs comprise the Yingshan Formation (O_{1-2y}) and the Yijianfang Formation (O_{2yj}). A comprehensive analysis was conducted, involving molecular components, carbon isotope composition, and a detailed examination of petroleum geochemical characteristics and secondary processes within the study area. Furthermore, the period and time of petroleum filling events were determined by combining inclusion homogenization temperature and burial-thermal history data. The study also analyzed the influence of various secondary processes on petroleum and identified the main factors controlling petroleum accumulation. This detailed characterization and analysis of the complex petroleum accumulation process in the ultra-deep Tarim Basin provide valuable insights for future exploration endeavors in ultra-deep petroleum.

2. Geological setting

The Tarim Basin, a significant superimposed basin, comprises Paleozoic marine craton and Meso-Cenozoic continental formations. Its geological history spans four pivotal tectonic evolution stages (Chen et al., 2021). Initially, during the early Caledonian period, the basin underwent a paleo-uplift embryonic stage. This

phase transitioned into the mid-late Caledonian-early Hercynian stage, marked by further uplift formation. Subsequently, during the late Hercynian-Indosinian period, it entered the "fault-uplift" development stage. Finally, the basin underwent a Yanshanian-Himalayan adjustment and shaping phase. The interplay of multiple extrusions and tensile stress shaped the basin into its current diamond-shaped geomorphology (Fig. 1(a)).

Located in the Shuntuoguole (STGL) low uplift, the Shunbei Oilfield is nestled in the Taklimakan Desert. It lies between the Tabei and Tazhong uplifts to the north and south, and the Manjiaer and Awati depressions to the east and west, respectively (Fig. 1(b)). Recent research highlights the Cambrian Yuertusi Formation (Є_{1y}) as the primary source rock in this region (Zhu et al., 2020; Qiao et al., 2024a). Multi-stage inherited strike-slip faults, influenced by multi-stage compressive stress, controlled the migration and accumulation of petroleum (Ma et al., 2022).

An area of about 3.2×10^4 km², the STGL low uplift represents a stable tectonic unit. Its sedimentary strata show comprehensive development, with occasional missing strata noted within certain groups or segments (Fig. 1(c)). Within the Ordovician formations, including the Penglaiba Formation (O_{1p}), Yingshan Formation (O_{1-2y}), Yijianfang Formation (O_{2yj}), Qiaerbake Formation (O_{3q}), Lianglitage Formation (O_{3l}), and Sangtamu Formation (O_{3s}). Notably, the carbonate rocks of O_{2yj} and O_{1-2y} serve as primary targets for petroleum exploration, with burial depths ranging from 7200 to 8800 m. These formations show an unconformable contact with the upper Ordovician Series, and the O_{3q} formation is notably absent in certain areas (Fig. 2).

3. Samples and methods

3.1. Samples

Research focused on the F6, F8, F10, F12, F14, and F16 petroleum reservoirs in the Shunbei Oilfield was selected as the research object. A total of 18 natural gas samples, 19 oil samples, and 8 core samples were collected for analysis. Further details on sampling types and locations are available in Fig. 1(b). Subsequent analyses included molecular compounds, biomarkers, isotopic compounds, and inclusion homogenization temperature.

3.2. Methods

3.2.1. Gas analysis

Natural gas samples were subjected to analysis using an HP 6890 II gas chromatograph equipped with flame ionization and thermal conductivity detectors. Gas chromatography identified the hydrocarbon gas components present in the samples. Additionally, the stable carbon isotopes of the gas samples were measured using GC-IRMS (Gas Chromatography-Isotope Ratio Mass Spectrometry) with a carrier coupled to the HP 6890 II GC apparatus.

3.2.2. Oil analysis

The oil group components were separated using column chromatography, employing a traditional method. The sample underwent partitioning into asphaltene, saturated hydrocarbons, aromatic hydrocarbons, and non-hydrocarbon components using elution solvents such as petroleum ether, dichloromethane, and dichloromethane + methanol. Organic sulfur compounds (OSCs) were separated using a silver chromatographic column. The preparation involved dissolving AgNO₃ solution in distilled water and impregnating silica gel (200 mesh), followed by activation at 105 °C for 4 h. The separation column was first filled with silica gel impregnated with AgNO₃, followed by ordinary silica gel (in a 3:2 ratio). The silica gel column was moistened with *n*-hexane, and a

few drops of *n*-hexane were added to dissolve the sample. Then the sample was loaded on a silica gel column impregnated with silver nitrate. The saturated hydrocarbon, aromatic hydrocarbon and OSC were obtained by eluate with *n*-hexane, dichloromethane and acetone successively.

An Agilent 6890 GC instrument equipped with an HP-PONA quartz capillary column (50 m × 0.25 mm × 0.25 μm) was utilized for whole-oil analysis for the determination of light hydrocarbon components. The detailed temperature program was as follows: The initial oven temperature was maintained at 35 °C for 10 min. It was then increased to 60 °C at 0.5 °C/min. Finally, it was heated to 300 °C at 2 °C/min and held for 10 min.

Analysis of saturated hydrocarbons, aromatic hydrocarbons, diamondoids, and OSCs was conducted using gas chromatography-mass spectrometry (GC-MS) employing an Agilent 7890 GC/5975i MS system. A HP-PONA column (60 m × 0.25 mm × 0.25 μm) was utilized in the gas chromatograph. The analytical procedure involved initially heating the gas chromatograph to 60 °C and holding for 2 min, followed by increasing to 310 °C at a rate of 3 °C/min, with a subsequent hold for 5 min. The mass spectrometer operated at an electron ionization energy of 70 eV in the selected ion monitoring mode. Known concentrations of D50-C₂₄, D8-Dibenzothiophene, D16-Adamantan, and D16-Adamantan were added to saturated hydrocarbons, aromatic hydrocarbons, diamondoids, and thiadiazole, respectively, as internal standards. The quantification of saturated hydrocarbons, aromatic hydrocarbons, diamondoids, and thiadiazole was achieved by comparing peak areas in the selected reaction monitoring mode. Fig. S1 displays details of the internal standard mass chromatograms.

3.2.3. Phase analysis

PVTsim software was used to simulate the petroleum phase, as detailed in Qiao and Chen (2022). This simulation was based on gas composition, whole oil composition, crude oil density, and gas-oil ratio (GOR).

3.2.4. Fluid inclusion analysis

Polished core samples extracted from the Yijianfang and Yingshan Formations within the Shunbei Oilfield were utilized to prepare inclusion plates, each with a thickness of approximately 0.08 mm. Microscopic examination of fluid inclusions was carried out employing a Nikon-LV100 microscope, equipped with dual channels for both fluorescence and reflected transmission light, enabling detailed visualization of the inclusions. For the determination of homogenization temperature, a LinkAM-THMSG600 cold and hot platform was employed. This apparatus offers a broad temperature range spanning from −190 to 600 °C, with a high precision temperature measurement error of ±0.1 °C.

3.2.5. One-dimensional burial-thermal modeling

The burial and thermal histories of the SHB84X well in the Shunbei Oilfield were reconstructed using PetroMod software. Burial depth and stratigraphic age data were provided by SINOPEC Northwest Company (Urumqi), ensuring the accuracy and reliability of the modeling process. Initially, the heat flow value and formation denudation thickness, as reported by Li et al. (2022), were utilized as foundational parameters for the modeling endeavor. Subsequently, these parameters were subjected to adjusted and corrected according to the equivalent vitrinite reflectance (calculated according to the bitumen reflectance) and the reservoir temperature.

4. Results

4.1. Petroleum reservoir types and fluid properties

PVTsim software was utilized to simulate the *P-T* phase diagram, indicating that the F6, F8, F10, F12, F14, and F16 reservoirs primarily consist of condensate and gas reservoirs (Fig. 3(a)–(d)). The GOR (cumulative production gas-oil ratio) ranges from 1738 to 464814 m³/m³ (Table 1). The evolution law of the petroleum envelope highlights significant differences in the thermal evolution degree of petroleum (Fig. 3(a)–(d); Qiao and Chen, 2022).

The relative contents of the fluid components (C₁+N₂, C_{2–6}+CO₂, and C₇⁺) in the study area were 71.20%–94.45%, 5.34%–23.57%, and 0.02%–5.75%, respectively. These components are evenly distributed across condensate, wet gas, and dry gas reservoir regions, as shown in the ternary diagram (Fig. 3(e)).

The distribution of crude oil density in the study area ranges from 0.74 to 0.81 g/cm³, with an average value of 0.77 g/cm³ (Table 1). The viscosity ranges from 0.76 to 2.38 mm²/s, with an average of 1.36 mm²/s (Table 1). Overall, the oil is characterized by low sulfur (<0.5%) and low wax (<10%) content, exhibiting similar volumetric properties (Table 1).

4.2. Alkanes, terpanes, and steranes

The *n*-alkanes in the study area's oil samples are intact, with a distribution range from *n*-C₅ to *n*-C₃₂. The dominant peak carbon numbers ranged from C₅ to C₇, showing a unimodal distribution (Fig. 4(a1)–(d1)). Additionally, the ratios of Pr/*n*-C₁₇ and Ph/*n*-C₁₈ ranged from 0.06 to 0.23 and 0.05 to 0.27, respectively (Table 2). Both ratios were significantly below 1.0, with the isoprene content obviously lower than that of adjacent *n*-alkanes (Fig. 4(a1)–(d1)).

Fig. 4 illustrates significant differences in the distribution characteristics of terpenes (*m/z* 191) and steranes (*m/z* 217) in oil samples from the study area. Biomarkers underwent varying degrees of decomposition, and the baseline of the mass chromatography was shifted to different degrees. Notably, SHB6X oil exhibited complete decomposition of steranes and terpenes. Additionally, 25-norhopane was detected in the majority of oil samples (Fig. 5).

4.3. Light hydrocarbons and diamondoids

Light hydrocarbon compounds, mainly alkanes, were identified in the C₃–C₇ range, followed by cycloalkanes and aromatics (Fig. 6). Table 2 presents key parameters derived from the analysis of these compounds. Moreover, the oil samples show abundant diamondoid compounds, with total concentrations ranging from 1761.22 μg/g to 62187.88 μg/g. Table 3 provides essential parameters derived from the analysis of diamondoid components.

4.4. Thiadiazole

Thiadiazole, sulfur-containing non-hydrocarbons, were isolated using a silver chromatographic column and analyzed via gas chromatography-mass spectrometry. Thiadiazole were confirmed in oil samples from the study area (Fig. 7). The total thiadiazole concentrations in the oil samples ranged from 0.14 to 23.80 μg/g, with thiaadamantanes being predominant components (Fig. 7 and Table 3).

4.5. Composition and stable carbon isotope of natural gas

The samples primarily contain hydrocarbon gas, with molar concentrations exceeding 86% (Table 4). Specifically, methane content in gas samples from the study area ranges from 73.23% to

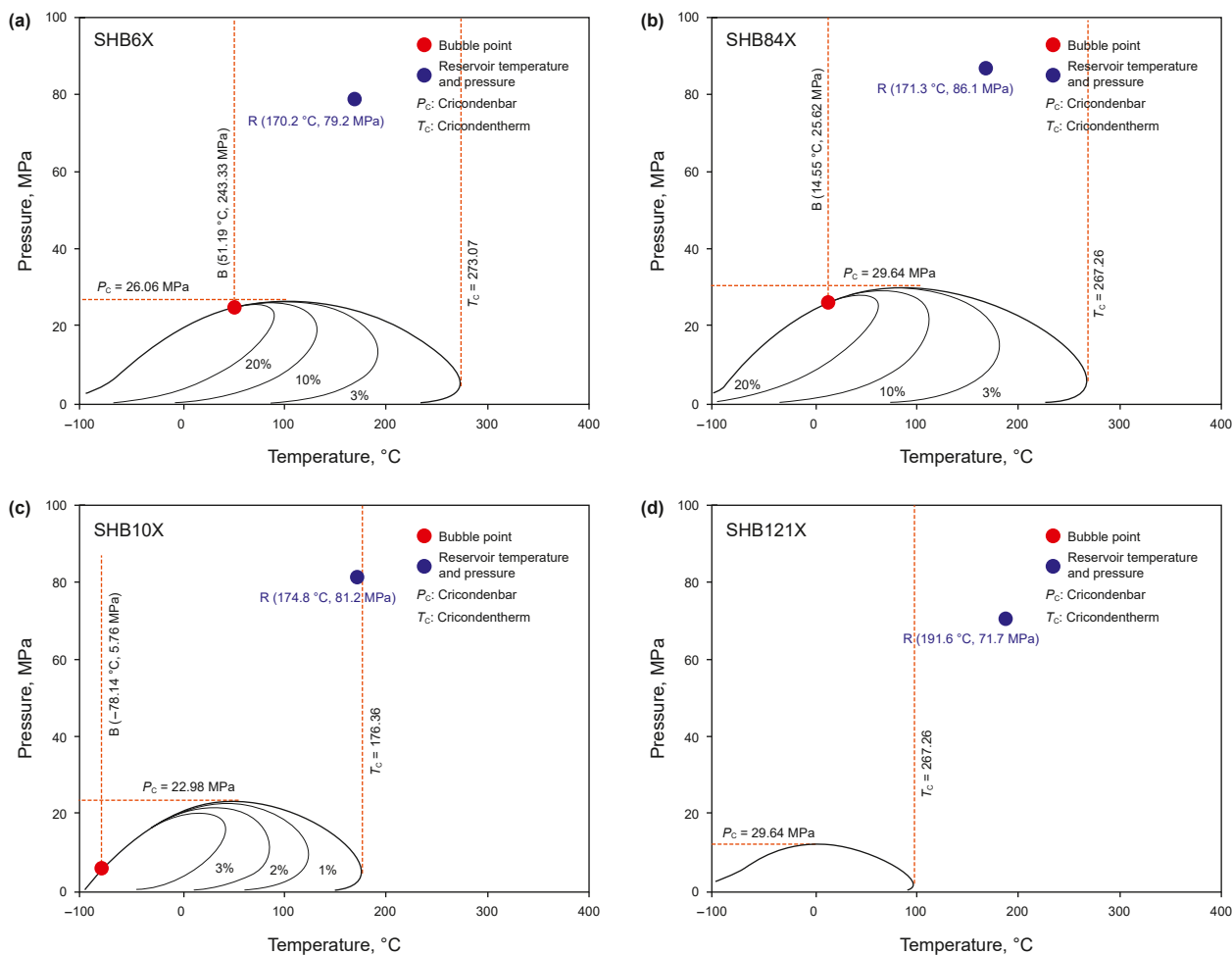


Fig. 3. PVT phase diagrams (a, b, c, d) and three-terminal diagram of fluid components (e) of the Shunbei Oilfield.

Table 1 Physical properties and fluid component parameters of oils in the Shunbei Oilfield.

Area	Well	Strate	Depth, m	P_R , MPa	T_R , °C	GOR, m ³ /m ³	Density, g/cm ³	Viscosity, mm ² /s	Sulfur, %	Wax, %	C ₁ +N ₂ %	C ₂₋₆ +CO ₂	C ₇ ⁺	
F6	SHB61X	O ₂ yj + O ₁₋₂ y	7726	8544	91.3	173.7	1738	0.77	1.31	0.02	2.40	71.20	23.05	5.75
	SHB6X	O ₂ yj + O ₁₋₂ y	7742	8132	79.2	170.2	1938	0.76	1.60	0.06	3.90	73.85	20.80	5.35
F8	MS8	O ₂ yj + O ₁₋₂ y	—	—	87.5	168.4	2800	0.76	1.34	0.02	2.50	84.41	11.61	3.98
	SHB85X	O ₂ yj + O ₁₋₂ y	8033	8832	65.1	171.3	2000	0.76	1.56	0.10	1.40	77.21	18.10	4.69
	SHB84X	O ₂ yj + O ₁₋₂ y	8400	9195	86.1	171.3	2040	0.76	1.47	0.09	1.30	81.87	12.92	5.21
	SHB83X	O ₂ yj + O ₁₋₂ y	7821	8478	74.1	173.6	3826	0.76	1.56	0.10	1.40	71.23	23.57	5.20
	SHB802X	O ₂ yj + O ₁₋₂ y	8250	8397	87.6	170.9	6627	0.75	1.56	0.03	3.40	90.19	8.24	1.57
	SHB8X	O ₂ yj + O ₁₋₂ y	7737	7740	61.7	182.6	3670	0.76	1.07	0.01	0.21	87.88	11.24	0.88
	SHB8-2H	O ₂ yj + O ₁₋₂ y	7693	8854	62.6	176.5	2566	0.76	2.38	0.06	1.60	84.92	11.61	3.47
	SHB801X	O ₂ yj + O ₁₋₂ y	7691	9145	70.0	177.3	7740	0.78	1.75	0.16	2.80	89.94	8.55	1.51
	SHB8-3H	O ₂ yj + O ₁₋₂ y	7759	8531	86.7	176.1	5658	0.75	1.14	0.06	2.70	88.59	9.64	1.77
	SHB803X	O ₂ yj + O ₁₋₂ y	7661	8110	96.2	169.9	8542	0.75	1.14	0.06	2.70	88.91	9.86	1.23
	SHB82X	O ₂ yj + O ₁₋₂ y	7617	8262	88.2	177.2	4831	0.76	0.76	1.39	0.27	88.72	9.74	1.54
	SHB804X	O ₂ yj + O ₁₋₂ y	7599	8343	87.9	178.0	62135	0.80	1.71	0.02	3.50	94.45	5.34	0.21
F10	SHB10X	O ₂ yj + O ₁₋₂ y	7809	8591	81.2	174.8	4299	0.74	2.03	0.15	2.60	84.37	13.15	2.48
F12	SHB122X	O ₂ yj + O ₁₋₂ y	7290	8520	54.0	193.1	197787	0.80	0.77	0.53	0.03	87.60	12.35	0.05
	SHB12X	O ₂ yj + O ₁₋₂ y	7126	8121	69.5	191.5	148448	0.81	0.78	0.50	0.06	88.92	11.00	0.08
	SHB121X	O ₂ yj + O ₁₋₂ y	7527	8287	71.7	191.6	464814	0.79	0.78	0.61	0.06	88.39	11.59	0.02
F14	SHN1	O ₂ yj + O ₁₋₂ y	6528	6690	75.4	180.1	86723	0.80	1.15	0.14	0.38	83.34	16.50	0.16

GOR = cumulative produced gas to oil ratio; P_R = Formation pressure; T_R = Formation temperature.

94.51%, with an average of 86.83% (Table 4). Additionally, the dryness coefficient ranges from 0.77 to 1.00, averaging 0.94, indicating a transition from wet to dry gas from north to south (Table 4). The

$\delta^{13}C_1$ values range from -44.60‰ to -36.80‰, with an average of -40.80‰ (Table 4).

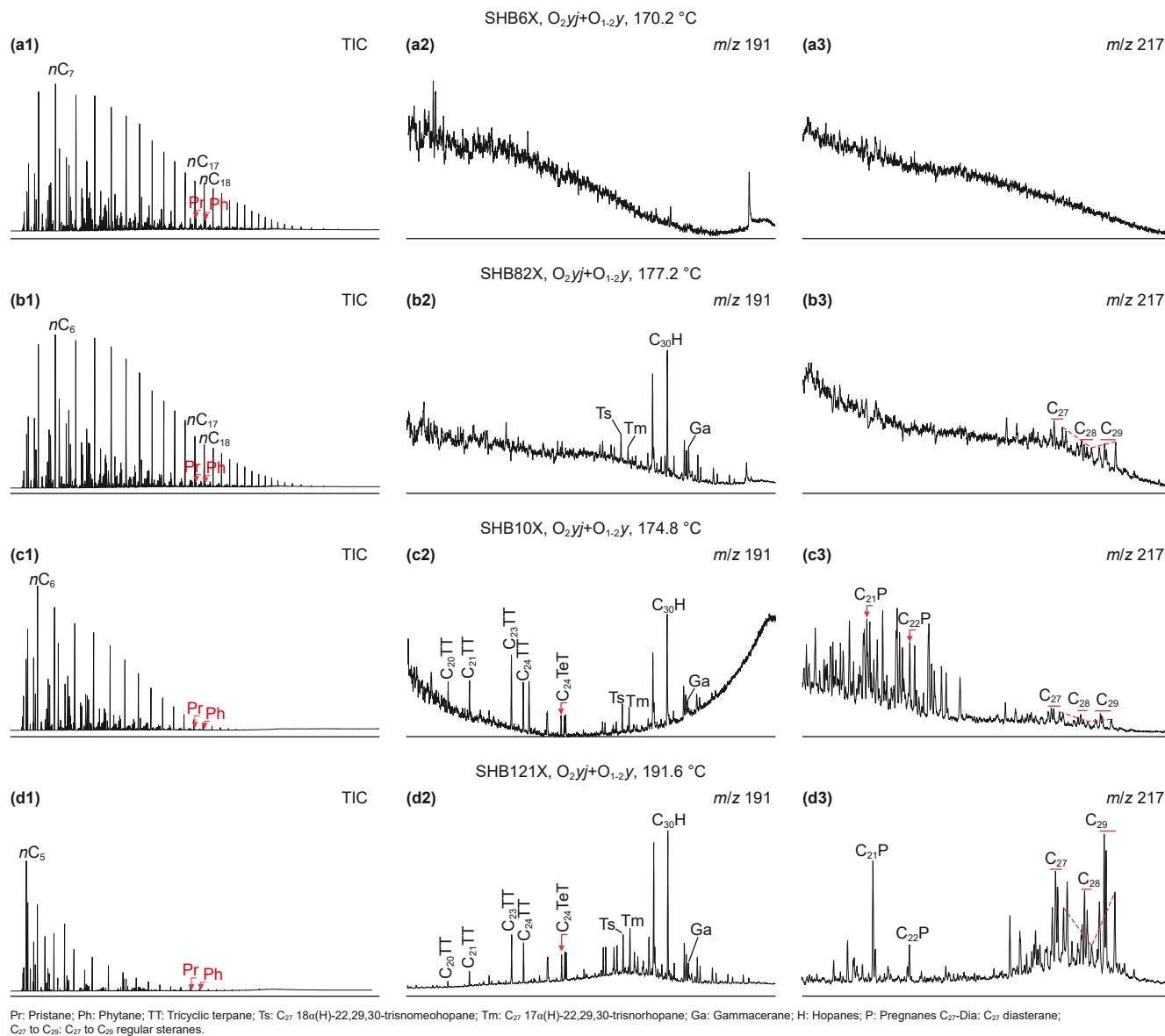


Fig. 4. Representative TIC ((a1)–(d1)), m/z 191 mass chromatograms ((a2)–(d2)) and m/z 217 mass chromatograms ((a3)–(d3)) from the Shunbei Oilfield.

5. Discussion

5.1. Organic matter input and source

Light hydrocarbons play a crucial role in petroleum, often constituting over 90% of light oil (Hunt et al., 1980). These compounds, abundant in genetic information, have been widely used in petroleum correlation studies (Hunt, 1984; Hu et al., 1990; Qiao et al., 2022; Deng et al., 2023; Fig. 8(a) and (b)). The relative contents of cyclohexane (CH) and methylcyclohexane (MCH) in oil samples ranged from 9.54% to 24.78% (<30%) and 15.56%–38.93% (<50%), respectively (Table 2). Fig. 7 shows that sapropelic parent materials such as plankton, benthic algae, and bacteria are the primary inputs.

Schulz et al. (2001) observed that 3,4-dimethyldiamantane (DMD) is enriched in coal and mudstone with type III organic matter, while 4,8-DMD and 4,9-DMD are found in carbonate rocks and marine siliciclastic rocks with type I and II organic matter, respectively. As a result, DMDI-1 ($100 \times 3,4-/3,4-+4,9-$ DMD) and

EAI ($100 \times 2-/2-+1$ -EA) were utilized to determine the parent material type. The cross-plot of DMDI-1 and EAI reveals that marine type II organic matter is the primary input (Fig. 8(c)).

The distribution ranges of Pr/ n -C₁₇ and Ph/ n -C₁₈ in oil samples range from 0.06 to 0.23 and from 0.05 to 0.27, respectively, with average values of both around 0.15 (Table 2). According to a cross-plot analysis, the oil's source kitchen is formed in a marine reduction environment, with the primary parent material sources being Algal type II (Fig. 7(a); Shanmugam, 1985).

Various wells (e.g., LT1, XH1, and TS5) and outcrops indicate that a set of high-quality marine source rocks developed in the Lower Cambrian strata (Zhu et al., 2020, 2021). The oil source (Cambrian-Lower Ordovician or Middle-Upper Ordovician) in the Tarim Basin has been widely discussed in previous studies (Zhang et al., 2022). However, previous studies have mostly suggested, based on biomarker, carbon isotope, and sulfur isotope analyses, that marine petroleum in the Tarim Basin primarily originates from the Lower Cambrian source rocks (Cai et al., 2015; Wang et al., 2021).

In summary, Lower Cambrian marine shales are proposed as the

Table 2
Biomarker and light hydrocarbon parameters of oils in the Shunbei Oilfield.

Well	Pr/nC ₁₇ *	Ph/nC ₁₈ *	K ₁ *	H*	I*	B*	F*	n-C ₆ *	MCP*	CH*	n-C ₇ *	ΣDMCP*	MCH*	DBTs	αααC ₂₉ 20R
								%			%				
SHB61X	0.22	0.27	1.09	39.70	3.52	0.42	2.05	74.20	9.12	16.68	60.49	9.96	29.55	219.55	0.03
SHB6X	0.23	0.23	1.09	40.22	3.52	0.46	1.99	71.58	9.74	18.68	60.02	9.81	30.17	176.64	0.00
MS8	0.18	0.19	1.13	33.71	2.75	0.66	1.27	62.73	12.49	24.78	49.42	11.65	38.93	509.82	0.54
SHB85X	0.19	0.18	1.12	35.31	2.26	0.41	1.40	67.06	13.36	19.58	51.44	11.83	36.73	142.44	0.00
SHB84X	0.21	0.21	1.14	35.80	3.19	0.43	1.56	71.16	10.34	18.50	54.37	10.69	34.94	23.75	0.69
SHB83X	0.18	0.18	1.13	34.83	3.23	0.45	1.57	72.75	10.55	16.70	54.31	11.15	34.54	218.02	0.12
SHB802X	0.14	0.14	1.10	39.48	3.43	0.65	1.68	67.97	11.72	20.31	56.53	9.73	33.74	161.31	0.00
SHB8X	0.10	0.10	1.10	40.81	4.13	0.52	1.84	72.75	9.79	17.46	59.33	8.47	32.20	69.90	0.00
SHB8-2H	0.16	0.16	1.16	38.91	4.42	0.39	1.75	77.48	6.82	15.70	58.42	8.17	33.41	24.83	0.00
SHB801X	0.09	0.07	1.16	46.55	4.97	0.55	1.99	70.76	7.65	21.59	62.50	6.03	31.47	45.32	0.07
SHB8-3H	0.10	0.08	1.19	40.22	5.01	0.42	2.00	81.44	6.37	12.19	61.60	7.59	30.81	13.50	0.01
SHB803X	0.08	0.08	1.24	39.84	6.04	0.40	2.08	81.74	5.46	12.80	62.73	7.17	30.10	31.06	0.02
SHB82X	0.06	0.05	1.21	39.03	5.42	0.38	1.88	76.39	6.60	17.01	60.26	7.70	32.04	96.04	0.56
SHB804X	0.07	0.07	1.37	44.31	5.57	0.89	3.39	82.73	6.64	10.63	70.66	8.53	20.81	213.67	0.00
SHB10X	0.14	0.12	1.23	36.52	6.35	0.33	1.54	80.56	5.23	14.21	56.57	6.57	36.86	2.44	0.27
SHB122X	0.19	0.20	1.32	28.96	5.30	4.33	1.42	70.08	7.69	22.23	53.38	9.08	37.54	108.23	97.23
SHB12X	0.22	0.24	1.27	31.42	4.54	3.97	1.68	69.20	8.66	22.14	56.90	9.13	33.97	29.71	20.40
SHB121X	0.12	0.16	1.30	43.40	8.98	1.37	5.06	86.35	4.11	9.54	78.51	5.93	15.56	179.23	27.30
SHN1	0.11	0.13	1.31	43.78	7.99	1.10	3.96	71.12	14.44	14.44	57.66	12.97	29.37	1169.35	5.00

CH = cyclohexane; MH = methylhexane; MCH = methylcyclohexane; Tol = toluene; nC₇ = n-heptane; DMP = dimethylpentane; DMCP = dimethylcyclopentane; K₁ = (2-MH+2,3-DMP)/(3-MH+2,4-DMP) (Mango, 1997); I = Isoheptane value (Isoheptane Value = (2 + 3)-MH/(1c3 + 1t3 + 1t2)-DMCP), H = Heptane value (Heptane Value = (nC₇ × 100)/(CH + 2-MH + 2,3-DMP + 1,1-DMCP + 3-MH + 1c3-DMCP + 1t3-DMCP + 1t2-DMCP + nC₇ + MCH)) (Thompson, 1983); B = Tol/nC₇; F = nC₇/MCH; ΣDMCP = (1,1 + cis-1,3+trans-1,3+trans-1,2)-DMCP; * = data from Whole-oil GC analysis.

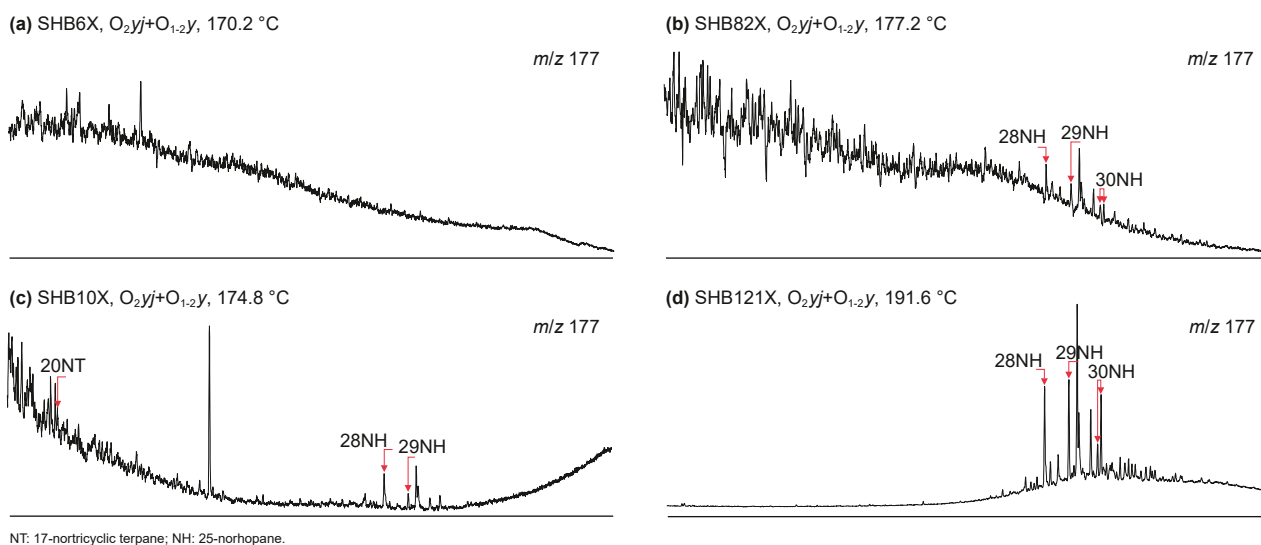


Fig. 5. Representative *m/z* 177 mass chromatograms ((a)–(d)) from the Shunbei Oilfield.

primary contributors to the petroleum reservoirs in the Ordovician of the Shunbei Oilfield.

5.2. Maturity assessment of oil

Maturity is crucial for assessing oil properties, predicting oil-gas conversion, and characterizing oil formation stages (Mackenzie et al., 1980). The chemical composition of oil formed in different thermal evolution stages of source rocks is obviously varies (Wilhelms and Larter, 2004). Light hydrocarbon and diamondoid components, particularly abundant in high thermal evolution stages, play a significant role in assessing oil maturity (Wang et al., 2021; Qiao et al., 2022).

Analysis of heptane and isoheptane values indicates the high maturity stage of oil in the study area, with type II kerogen as the primary source of organic matter (Thompson, 1983). Walters et al.

(2003) proposed a method for calculating equivalent vitrinite reflectance (*R_c*) based on cross-plots of heptane and isoheptane values, indicating that the *R_c* of oil in the study area exceeds 1.1% (Fig. 9).

Diamondoid compounds in oil can undergo varying degrees of loss and enrichment due to evaporative fractionation, affecting the reliability of maturity evaluation results (Moldowan et al., 2015; Qiao et al., 2024b). Nevertheless, the oil samples in the study area exhibit a robust linear relationship between 1-+2-methyladamantane (1-+2-MA) and 3-+4-methyldiamantane (3-+4-MD), with $R^2 = 0.9925$ (Fig. 10(a)). This indicates that diamondoid components in the oil are unaffected by evaporative fractionation, thus serving as reliable maturity indicators. The cross-plot of the methyladamantane index (MAI) and the methyldiamantane index (MDI) confirms the oil's high maturity stage, with equivalent vitrinite reflectance exceeding 1.3% (Fig. 10(b));

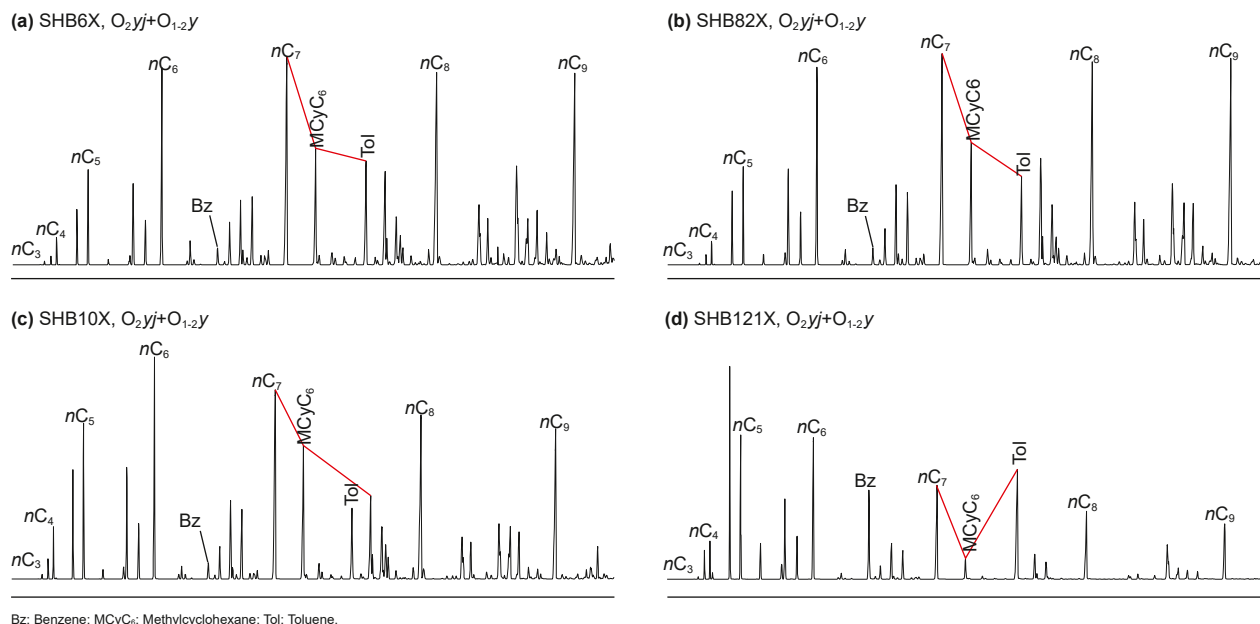


Fig. 6. Gas chromatograms of light hydrocarbons ((a)–(d)) from the Shunbei Oilfield.

Table 3
Diamondoid and thiaadamantoid parameters of oils in the Shunbei Oilfield.

Well	1+2-MA	4+3-MD	TAs	Ts	MAI	MDI	DMDI-1	EAI	Rc	EOC1	EOC2
	μg/g	μg/g	μg/g	μg/g	%						
SHB61X	363.00	40.42	0.32	0.40	75.26	43.04	64.28	50.12	1.48	50.51	33.69
SHB6X	432.37	49.82	0.19	0.22	76.53	43.94	64.02	46.58	1.51	59.85	45.27
MS8	624.02	76.14	–	–	75.99	43.84	65.03	46.58	1.50	73.73	62.49
SHB85X	386.97	46.53	–	–	73.02	40.45	67.99	49.72	1.42	57.01	41.75
SHB84X	450.84	53.03	–	–	75.92	45.61	64.59	47.95	1.55	62.28	48.29
SHB83X	498.42	56.51	21.78	23.80	76.67	42.69	66.96	46.18	1.48	64.61	51.18
SHB802X	1107.44	122.39	0.84	1.02	79.85	45.09	64.48	38.94	1.53	83.66	74.80
SHB8X	999.72	111.88	0.65	0.85	79.93	45.25	63.32	38.99	1.54	82.12	72.89
SHB8-2H	571.68	49.96	1.22	1.22	75.24	43.27	66.61	43.53	1.49	59.96	45.41
SHB801X	2273.34	317.41	0.75	1.25	83.2	48.45	58.58	27.18	1.62	93.7	87.25
SHB8-3H	1319.81	161.79	–	–	83.18	48.24	58.75	31.65	1.61	87.64	79.74
SHB803X	1289.10	148.50	–	–	79.42	46.43	63.22	33.14	1.57	86.53	78.36
SHB82X	1090.66	118.51	13.44	14.73	78.72	46.39	62.33	39.05	1.57	83.12	74.13
SHB804X	5102.66	746.35	8.73	14.45	88.33	57.78	41.42	23.35	1.84	97.32	91.74
SHB10X	1230.67	56.66	0.09	0.14	80.42	48.08	61.41	35.20	1.61	64.70	51.29
SHB122X	12609.64	1511.43	–	–	91.29	57.97	42.79	4.40	1.85	98.68	93.43
SHB12X	9069.92	1330.26	–	–	94.08	60.43	33.70	7.06	1.91	98.5	93.21
SHB121X	9818.06	1313.46	1.73	4.32	88.53	54.17	48.97	13.59	1.76	98.48	93.18
SHN1	17356.50	2298.00	–	–	65.00	64.00	64.00	61.00	1.99	99.13	93.99

TAs = total thiaadamantanes; Ts = total thiaadamantoids; MA = methyladamantane; MD = methylidiamantane; DMD = methylidiamantane; EA = ethyladamantane; MAI = 1-MA/(1-MA+2-MA), MDI = 4-MD/(1-MD+3-MD+4-MD), Rc = 0.4389 + 0.0243 × MDI (Chen et al., 1996); DMDI-1 = 3,4-DMD/(3,4-DMD + 4,9-DMD), EAI = 2-EA/(2-EA + 1-EA) (Schulz et al., 2001); EOC1 (extent of oil cracking 1) = (1 - c₀/c_m) × 100, c₀ = the concentration of 3+4-MD in the uncracked samples, c_m = the concentration of 3+4-MD in any sample (Dahl et al., 1999); EOC2 = 1.2402 × EOC1 - 8.952 (Peng et al., 2022); “–” = no data.

Chen et al., 1996). Further calculation based on MDI values shows the distribution of oil Rc ($Rc = 0.4389 + 0.0243 \times MDI$) ranging from 1.42% to 1.99% (Table 3; Chen et al., 1996).

5.3. Reservoir secondary alteration

The accumulation and preservation of ultra-deep petroleum involve various secondary alteration, including biodegradation, thermal alteration, cracking, thermochemical sulfate reduction, and evaporative fractionation (Krouse et al., 1988; Losh et al., 2002; Sun et al., 2005; Zhu et al., 2019; Wang et al., 2021). Accurately characterizing these secondary processes in petroleum reservoirs is crucial for studying petroleum accumulation and preservation

mechanisms.

5.3.1. Oil cracking

Oil samples exhibit a strong linear correlation between 1+2-MA and 3+4-MD, underscoring the reliability of diamondoid parameters in the study area (Fig. 10(a)). Dahl et al. (1999) observed an increase in the concentration of 3+4-MD with thermal cracking. Subsequently, the extent of oil cracking (EOC) was calculated using the concentration of 3+4-MD with the formula $EOC1 = (1 - c_0/c_m) \times 100$, where c₀ is the concentration of 3+4-MD in the uncracked samples (3+4-MD “baseline concentration”) and c_m is the concentration of 3+4-MD in any sample. The choice of baseline concentration for diamondoids significantly affects the reliability of

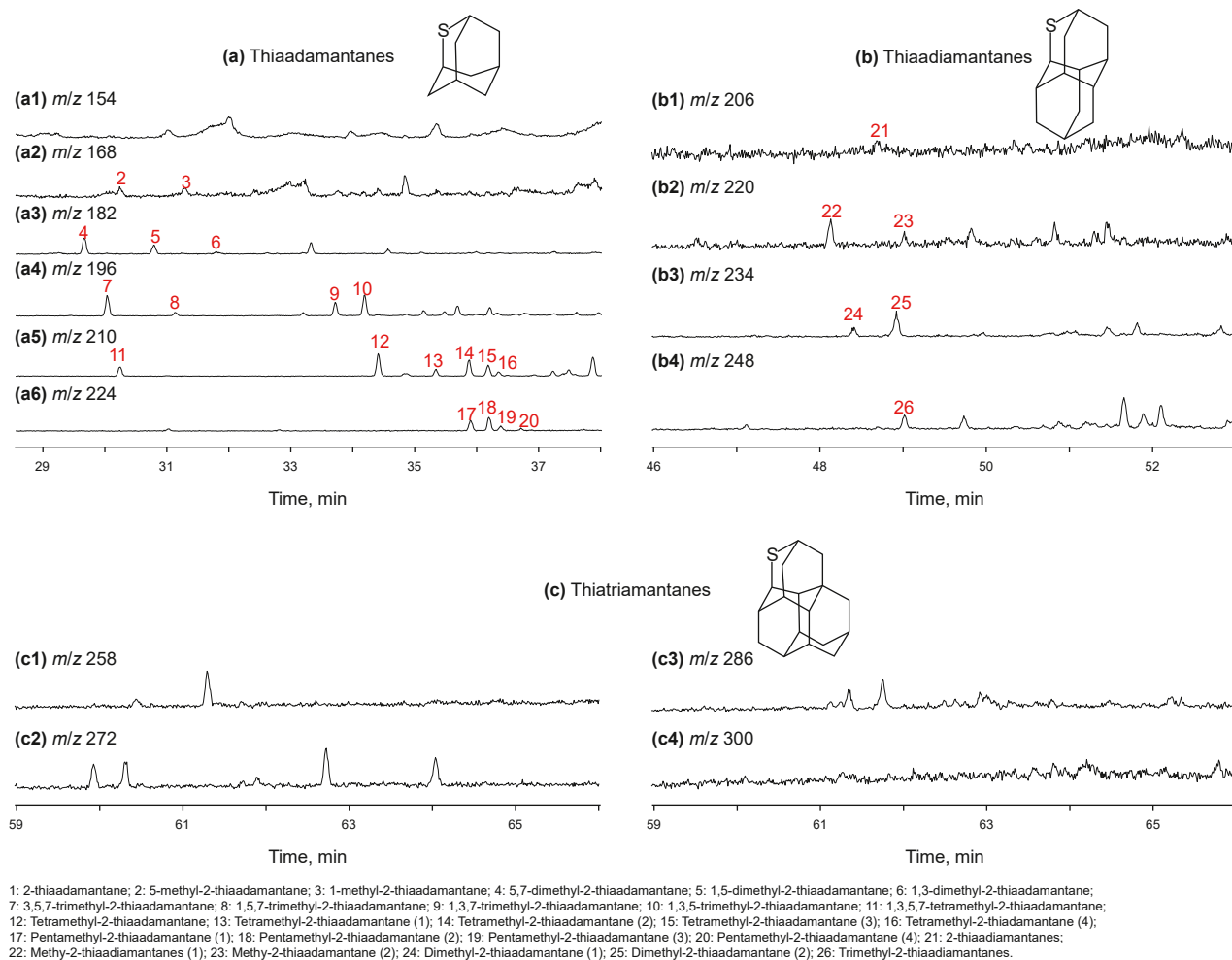


Fig. 7. Mass chromatograms of thiadiamondoids in oil from well SHB83X.

Table 4
Molecular and stable isotopic compositions of natural gas samples in the Shunbei Oilfield.

Well	Dryness	Molecular composition, mol %								$\delta^{13}\text{C}_{\text{PDB}}$, ‰			
		N_2	CO_2	C_1	C_2	C_3	$i\text{C}_4$	$n\text{C}_4$	$i\text{C}_5$	$n\text{C}_5$	C_1	C_2	C_3
SHB61X	0.77	2.84	1.80	73.23	8.34	5.32	0.21	3.60	2.30	2.36	—	—	—
SHB6X	0.80	1.67	2.43	77.10	7.57	5.14	1.80	2.75	0.78	0.76	—	—	—
SHB85X	0.92	5.57	1.88	85.57	3.76	1.59	0.48	0.65	0.24	0.25	−42.90	−31.10	−29.00
SHB84X	0.90	1.59	1.53	87.03	5.66	2.38	0.61	0.79	0.22	0.21	−42.10	−30.70	−28.50
SHB83X	0.91	1.51	2.14	87.24	5.12	2.19	0.60	0.78	0.22	0.19	−43.00	−29.90	−27.60
SHB801X	0.94	3.48	3.16	87.90	3.03	0.97	0.37	0.46	0.29	0.35	−42.50	−32.40	−31.00
SHB8-3H	0.94	1.06	3.10	89.99	3.50	1.07	0.35	0.43	0.23	0.28	−42.80	−30.10	−27.70
SHB803X	0.93	1.87	3.07	88.65	4.02	1.16	0.40	0.45	0.20	0.19	−44.60	−32.80	−30.70
SHB82X	0.93	0.72	2.71	89.47	4.48	1.25	0.42	0.51	0.22	0.22	−42.80	−32.30	−30.70
SHB804X	0.98	0.56	2.98	94.16	1.46	0.39	0.14	0.16	0.08	0.08	−40.20	−28.40	−26.30
SHB10X	0.90	1.49	2.59	86.04	6.35	1.92	0.57	0.61	0.22	0.20	−43.30	−31.80	−29.00
SHB122X	0.99	1.17	11.43	86.50	0.77	0.08	0.03	0.02	0.01	0.01	−39.80	−23.30	−22.20
SHB12X	1.00	0.51	10.65	88.49	0.30	0.03	0.01	0.00	0.00	0.00	−39.70	−29.50	−28.20
SHB121X	0.99	0.45	10.40	87.98	0.81	0.19	0.06	0.06	0.03	0.02	−39.10	−24.40	−21.00
SHN1	0.95	1.72	12.27	81.78	2.11	1.21	0.43	0.50	—	—	−38.30	−27.30	−23.80
SHN4	0.99	10.06	5.38	83.82	0.65	0.08	—	—	—	—	−37.80	−32.40	—
SHN5	1.00	3.41	1.97	94.51	0.11	0.01	—	—	—	—	−36.80	—	—
SHN7	1.00	6.19	0.28	93.42	0.10	0.01	—	—	—	—	−37.50	−27.40	—

Dryness = $\text{C}_1/(\text{C}_1 + \text{C}_2 + \text{C}_3 + \text{C}_4 + \text{C}_5)$, “—” = no data.

EOC calculations. A proposed “baseline concentration” of 20 $\mu\text{g/g}$ was chosen based on previous research and the characteristics of the oil samples (Wang et al., 2023; Qiao et al., 2024a).

The 4-+3-MD concentration in oil samples across the study area ranged from 40.42 to 2298.00 $\mu\text{g/g}$, generally decreasing from south to north (Table 3). Calculations reveal significant variations in

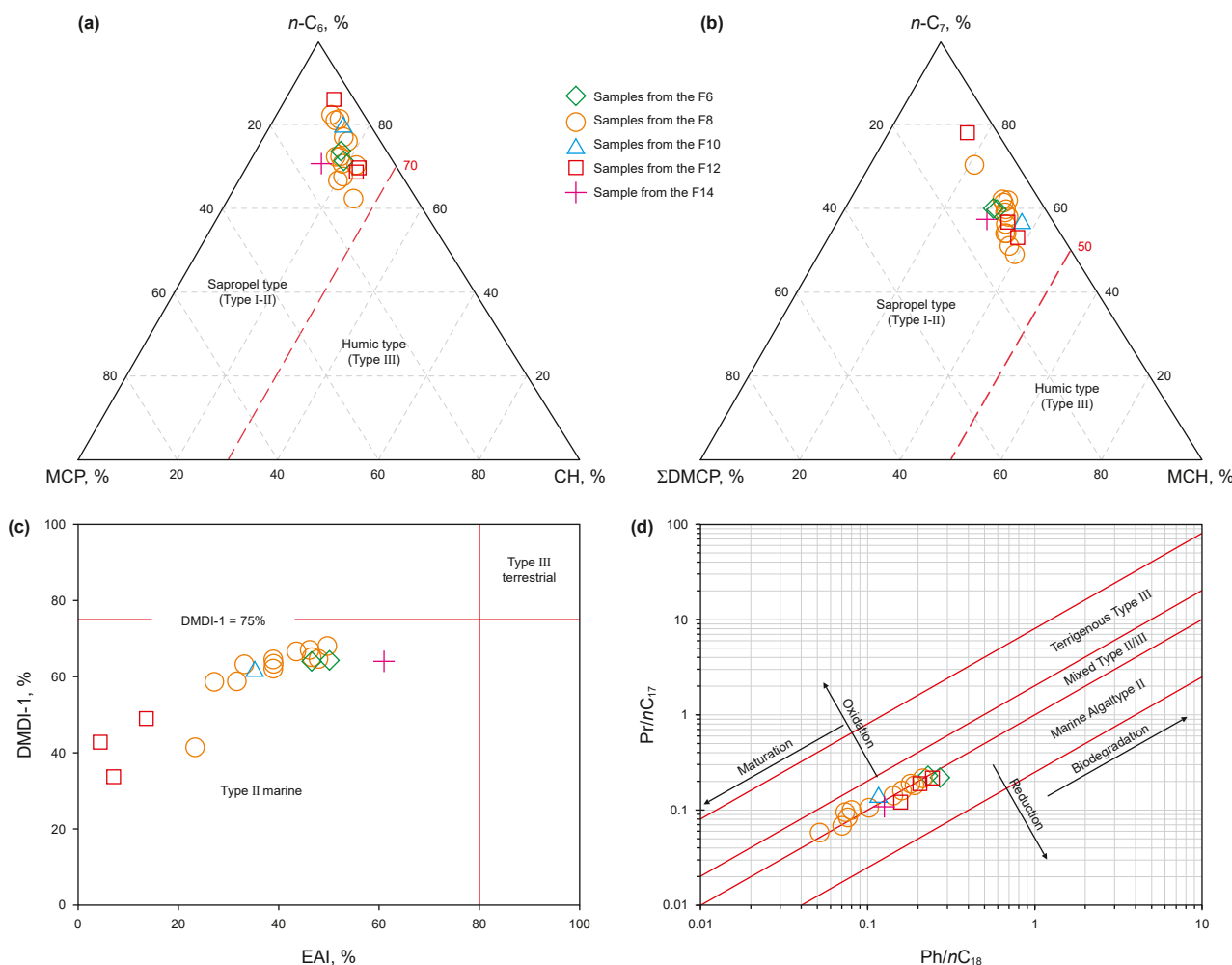


Fig. 8. Several diagrams identify sedimentary environments and sources of organic matter. (a): A triangle diagram of $n-C_6$, MCP, CH (refer to Hu et al., 1990); (b): A triangle diagram of $n-C_7$, $\Sigma DMCP$, and MCH (refer to Hu et al., 1990); (c): A cross-plot of DMDI-1 versus EAI (refer to Schulz et al., 2001); (d): A cross-plot of $Pr/n-C_{17}$ versus $Ph/n-C_{18}$ (refer to Shanmugam, 1985).

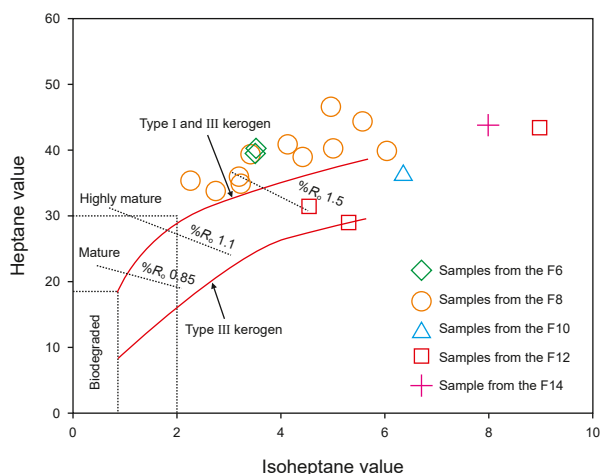


Fig. 9. A cross-plot of isoheptane value versus heptane value as indicators of thermal maturity and source organic type (refer to Thompson, 1983).

EOC among the oil samples, ranging from 50.52% to 99.13% (Table 3 and Fig. 11). MDI-based calculations indicate the R_c distribution

ranges from 1.42% to 1.99% (Table 3). When combined with the R_c result, it is observed that the calculated EOC in the study area may be overestimated. Peng et al. (2022) showed through simulations that at oil maturity levels of 1.2%–3.0%, the EOC calculated using 3+4-MD tends to be too high. A correction formula, $EOG_2 = 1.2402 \times EOC_1 - 28.952$, is proposed to improve the reliability of the calculated EOC. Further calculations reveal that the EOC in the study area ranges from 33.69% to 93.99% (Table 3). The EOC value in F12 exceeds 93%, indicating near-complete cracking of the oil. However, in the northern part of the study area, the EOC value is less than 62.5%, indicating it is still in the initial stage of oil cracking (Table 3).

5.3.2. Thermal alteration

The Tarim Basin has undergone extensive magmatic activity since the Paleozoic era. A key event was the formation of the Tarim Large Igneous Province (300–259 Ma) during the Permian (Xu et al., 2015; Zhu and Zhang, 2022). The widespread diabase intrusions during the Paleozoic (Xu et al., 2015), zircon U-Pb dating of diabase (Dong et al., 2013), in situ U-Pb dating of hydrothermal calcite (Xu et al., 2022), widespread barites, fluorites, and cherts in the reservoir (He et al., 2019), and positive Eu anomalies in the reservoir (Xu et al., 2022) all indicate that frequent magmatic intrusions and hydrothermal upwelling events occurred in the Tarim

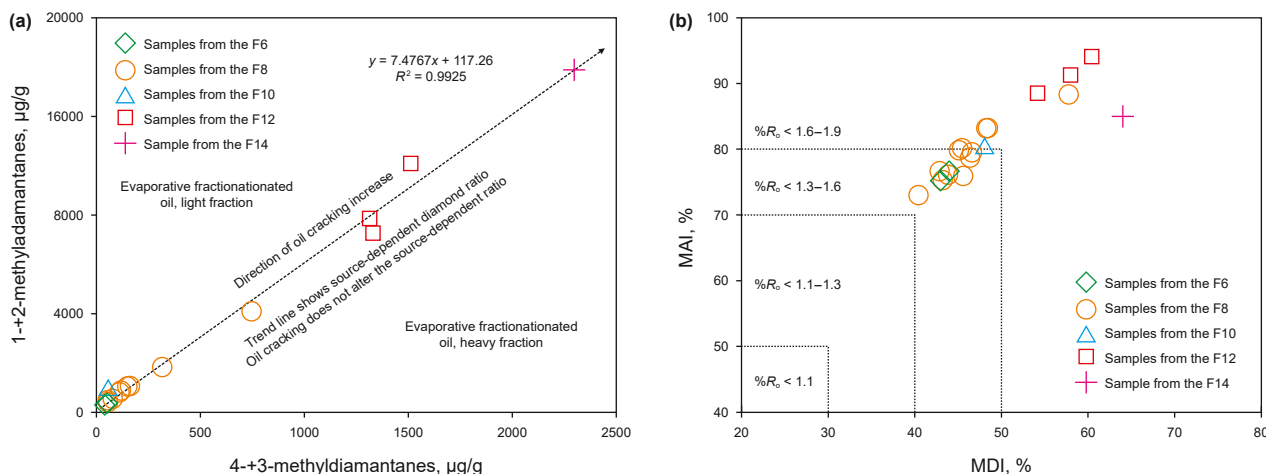


Fig. 10. A cross-plot of diamondoid concentrations and parameters. (a): A cross-plot of 1+2-methyladamantane concentrations versus 3+4-methyladamantane concentrations (refer to Moldowan et al., 2015); (b): A cross-plot of MAI versus MDI (refer to Chen et al., 1996).

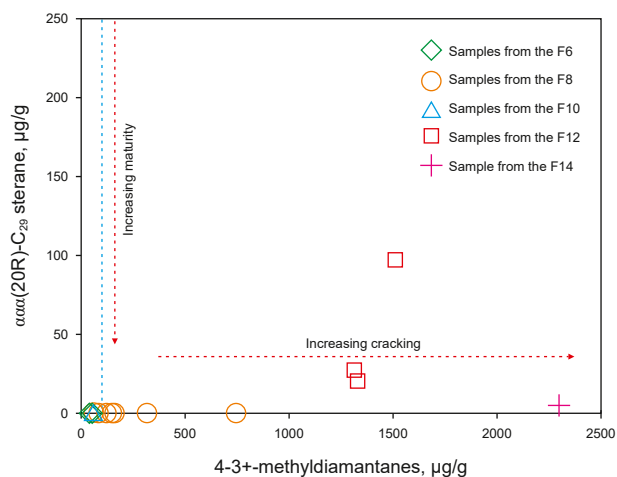


Fig. 11. A cross-plot of $\alpha\alpha\alpha(20R)-C_{29}$ sterane concentrations versus 3+4-methyladamantane concentrations (refer to Dahl et al., 1999).

Basin during the formation of the Large Igneous Province.

Multiple basement strike-slip faults have developed in the STGL Low Uplift (Fig. 1(b)). The fault was reactivated during the Permian, serving as a conduit for magma intrusion, hydrothermal upwelling, and petroleum migration (Ning et al., 2022). Previous studies have used carbon isotope values, polycyclic aromatic hydrocarbon enrichment, pyrobitumen distribution, and in situ U-Pb dating of hydrothermal calcite (295.90–283.00 Ma) to identify magmatic intrusions and hydrothermal upwelling in the Shunbei Oilfield (Wang et al., 2021; Xu et al., 2022; Li et al., 2023; Qiao et al., 2024a, 2025). These studies revealed varying degrees of thermal alteration in the petroleum reservoirs of the Shunbei Oilfield.

This is evidenced by the observation of intrusions of varying scales on seismic profiles. The distinct characteristics are identified by differences in seismic wave impedance between the intrusions and the surrounding rock (Fig. 12). The seismic profile shows that the igneous intrusions in the study area are primarily distributed between T_9^0 and T_4^1 and are located far from the reservoir (Fig. 12). Moreover, previous studies suggest that the thermal anomaly range caused by igneous intrusions is 1–2 times the size of the intrusion itself (Simoneit et al., 1978; Othman et al., 2001). This seems to suggest that the igneous intrusion in the study area has a limited

influence on the reservoir. However, unlike other regions, magma primarily intrudes upward along basement strike-slip faults in the Shunbei Oilfield. Magma rising from the deep basin can significantly influence the reservoir and create channels for subsequent hydrothermal upwelling and petroleum migration (Zhu and Zhang, 2022; Qiao et al., 2024a). Therefore, oil alteration in the reservoir caused by magmatic intrusion in the study area cannot be assessed solely according to the distribution range of igneous intrusion.

In normal geological evolution, reservoir temperature is usually positively correlated with the cracking degree. This correlation directly influences biomarker concentrations and the distribution characteristics of the spectral baseline. Higher reservoir temperatures typically result in more pronounced baseline drift and lower biomarker concentrations (Peters et al., 2005; Qiao et al., 2022). However, there is an obvious mismatch between biomarker distribution and reservoir temperature in the Shunbei Oilfield. For instance, reservoir temperatures in F6, F8, and F10 range from 168.4 to 182.6 °C, with spectra (m/z 191 and m/z 217) showing significant baseline drift and low biomarker concentration (Fig. 12(a3)–(c3); Table 1). Conversely, reservoir temperatures in F12 range from 191.5 to 193.1 °C, with spectra (m/z 191 and m/z 217) indicating a relatively stable baseline and intact biomarkers (Fig. 12(d3); Table 1).

Moreover, the EOC of F12 oils is significantly higher than that of F6 oils. Nonetheless, biomarkers in F12 oils exhibit superior preservation compared to F6 oils (Fig. 12(a3) and (d3)). The preceding analysis indicates that thermal anomalies (transient high temperatures) affected the biomarkers of F6, F8, and F10 oils, leading to significant cracking. In contrast, biomarkers in F12 oils remain well preserved, suggesting no influence from significant thermal anomalies. Moreover, the study suggests that the reliability of biomarkers can extend to temperatures of at least 190 °C in the absence of significant thermal anomalies.

5.3.3. Biodegradation and mixing

Biodegradation, a common secondary alteration in reservoirs, significantly impacts the physical properties and chemical composition of oil (Sun et al., 2005).

Whole-oil chromatography showed a full series of n -alkanes without obvious an undifferentiated complex mixture (UCM) (Fig. 4(a1)–(d1)). Mass spectrometry analysis at m/z 177, however, detected 25-norhopane series compounds (Fig. 5). Previous studies have suggested that 25-norhopane forms through microbial-

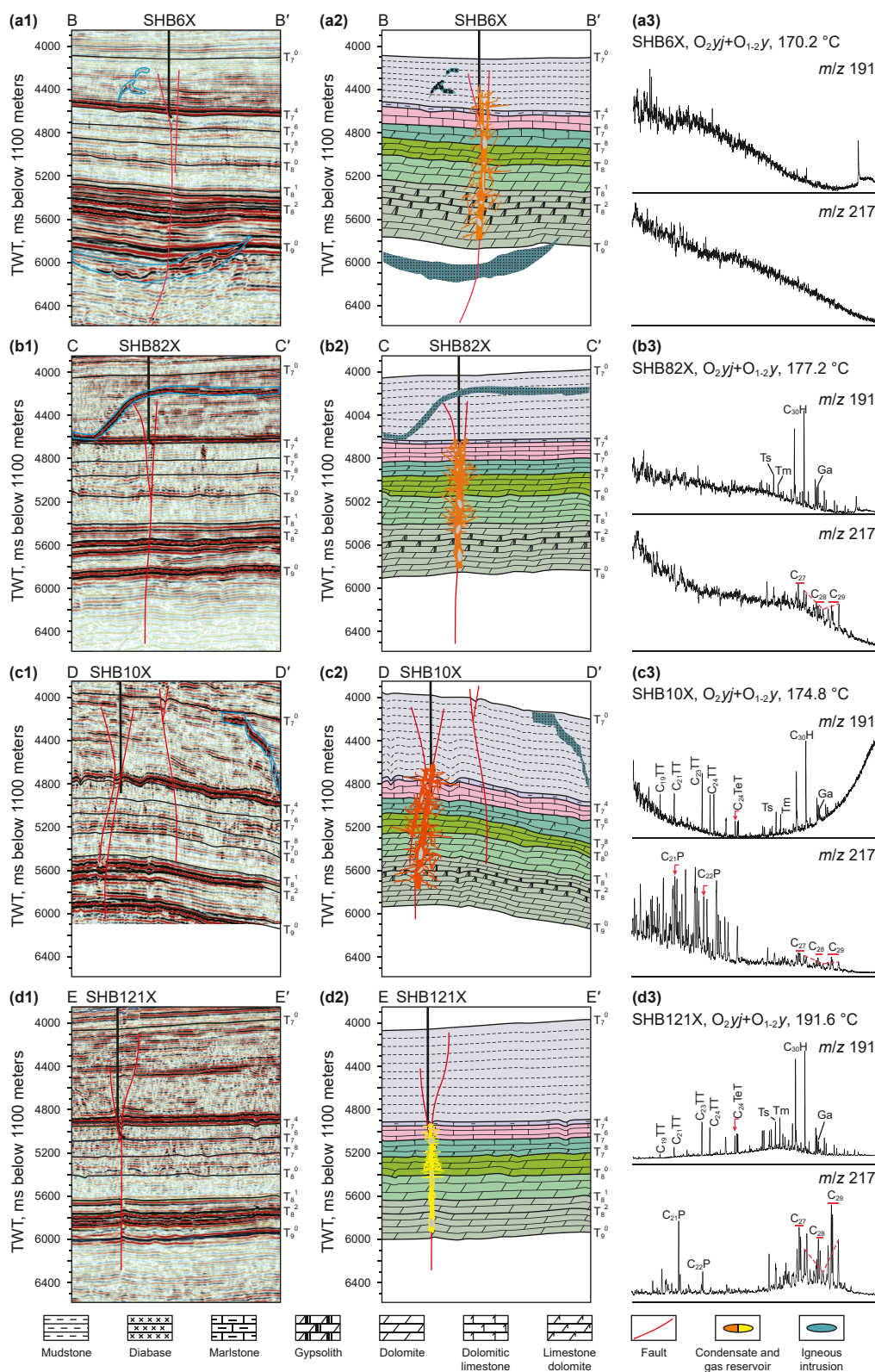


Fig. 12. Cross-well seismic section ((a1)–(d1)), relevant geological schematic section ((a2)–(d2)), and m/z 191 and m/z 217 mass chromatograms ((a3)–(d3)). See Fig. 1 for the direction of the seismic section.

induced demethylation of hopane (Moldowan and McCaffrey, 1995; Bennett et al., 2006). Therefore, the presence of 25-norhopane generally indicates a biodegradation level of at least 6 for

petroleum (Peters and Moldowan, 1993). During biodegradation, n -alkanes are typically depleted first (Peters et al., 2005). The coexistence of 25-norhopane and intact n -alkanes in the oil samples

suggests a mixture of early biodegraded oil and subsequently filled fresh oil in the study area (Zhu et al., 2019). However, F6 oils lacked 25-norhopane, likely due to the influence of Permian hydrothermal activity and complete cracking (Fig. 5(a)).

5.3.4. Thermochemical sulfate reduction

Previous studies have shown high H₂S levels (>8%) in Ordovician and Cambrian reservoirs within the Tarim Basin (Cai et al., 2001; Li et al., 2017). High H₂S content in deep basin reservoirs is typically attributed to thermochemical sulfate reduction (TSR) (Krouse et al., 1988). Gypsum-salt layers are extensively present in the Cambrian of the Tarim Basin, conducive to TSR. However, in Ordovician reservoirs lacking such layers, sulfate in formation water is believed to provide the necessary reactants for TSR. However, uncertainty remains regarding the occurrence of TSR in the Shunbei Oilfield Ordovician reservoirs (Wang et al., 2021).

In this study, detailed analyses of light hydrocarbon parameters, organic sulfur compound contents, and thiadiazolones were conducted to identify TSR in Ordovician reservoirs. The K₁ (K₁ = (2-methylhexane (MH) + 2,3-dimethylpentane (DMP))/(3-MH + 2,4-DMP)) values of the oils in the study area range from 1.09 to 1.37, all exceeding 1 (Table 2), indicating the potential occurrence of TSR (Mango, 1997). However, the distribution characteristics of 2-

MH+2,3-DMP and 3-MH+2,4-DMP significantly differ from those observed in oils affected by TSR in the Tazhong area (Fig. 13(a)). Further analysis, combined with K₁ values and concentrations of total dibenzothiophene series compounds (DBTs), revealed significantly lower DBTs concentrations in the oils of the study area compared to those in the oils affected by TSR in the Tazhong area (Fig. 13(b); Song et al., 2017).

Thiadiazolone detection revealed generally low levels in the study area (Table 3 and Fig. 13(c)), indicating a limited presence. Previous research suggests that oils may have undergone TSR when total thiaadamantanes (TAs) and thiadiazolones levels exceed 20 and 28 µg/g, respectively (Cai et al., 2016a, 2016b). Analysis of TAs and total thiadiazolones in oil samples indicated levels below 20 and 28 µg/g, respectively (Table 3 and Fig. 13(d)), confirming the absence of TSR. Only SHB83X shows a TAs content of 21.78 µg/g, slightly exceeding the threshold of 20 µg/g (Table 3 and Fig. 13(d)). Additionally, there is a predominance of thiaadamantanes in the detected thiadiazolones, with most samples solely containing thiaadamantanes and thiaadamantanes (Table 3 and Fig. 7), which suggests their origin in potential petroleum reservoirs affected by TSR in the Cambrian or source rocks (Gvirtzman et al., 2015; Wang et al., 2021).

Gypsum-salt layers are lacking in the Ordovician strata of the

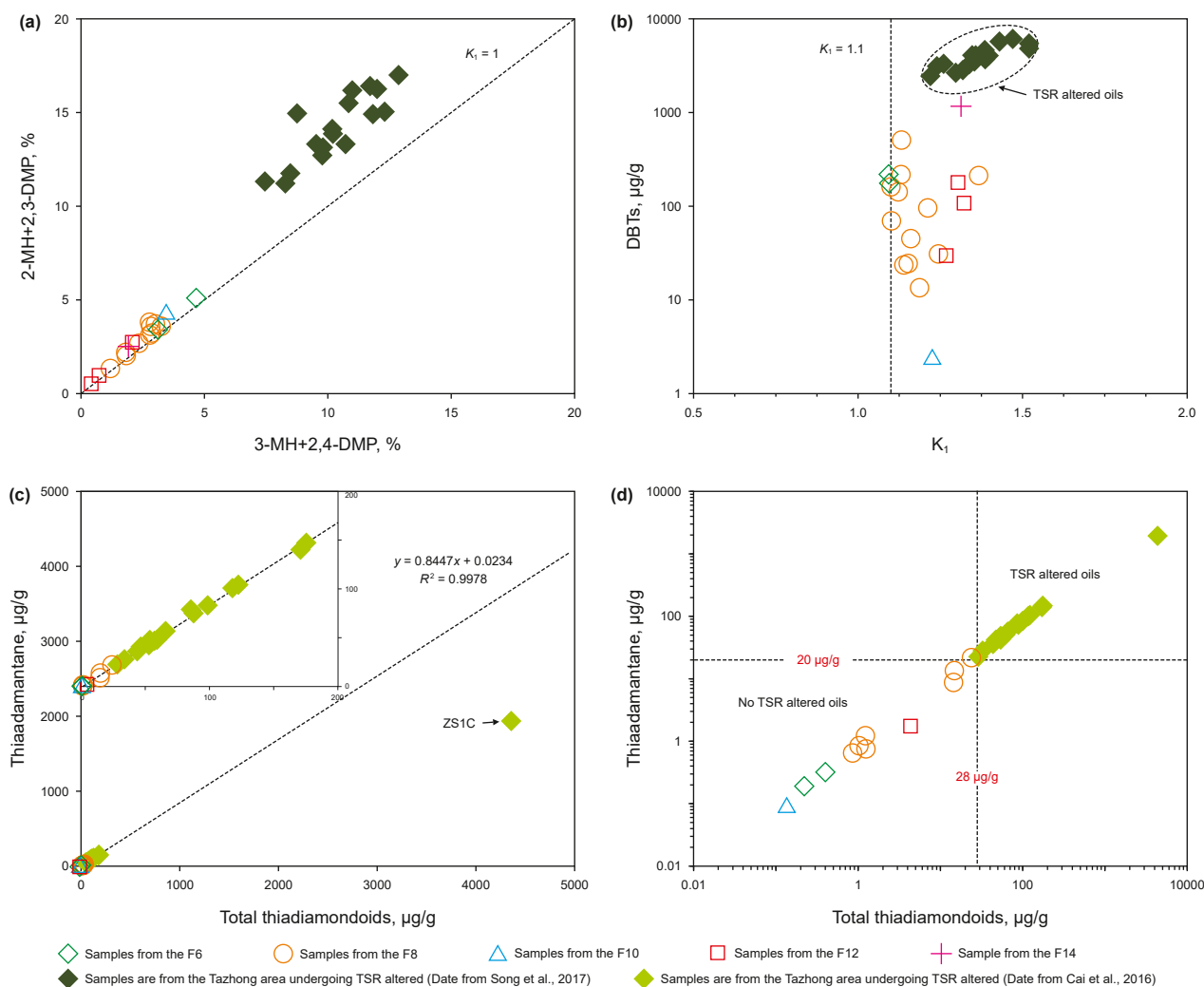


Fig. 13. A cross-plot of TSR identification. (a): A cross-plot of 2-MH+2,3-DMP versus 3-MH+2,4-DMP (refer to Mango, 1987); (b): A cross-plot of DBTs versus K₁ (refer to Song et al., 2017); (c) and (d): A cross-plot of total thiaadamantane concentrations versus total thiadiazolones concentrations (Tazhong date from Cai et al., 2016a, 2016b).

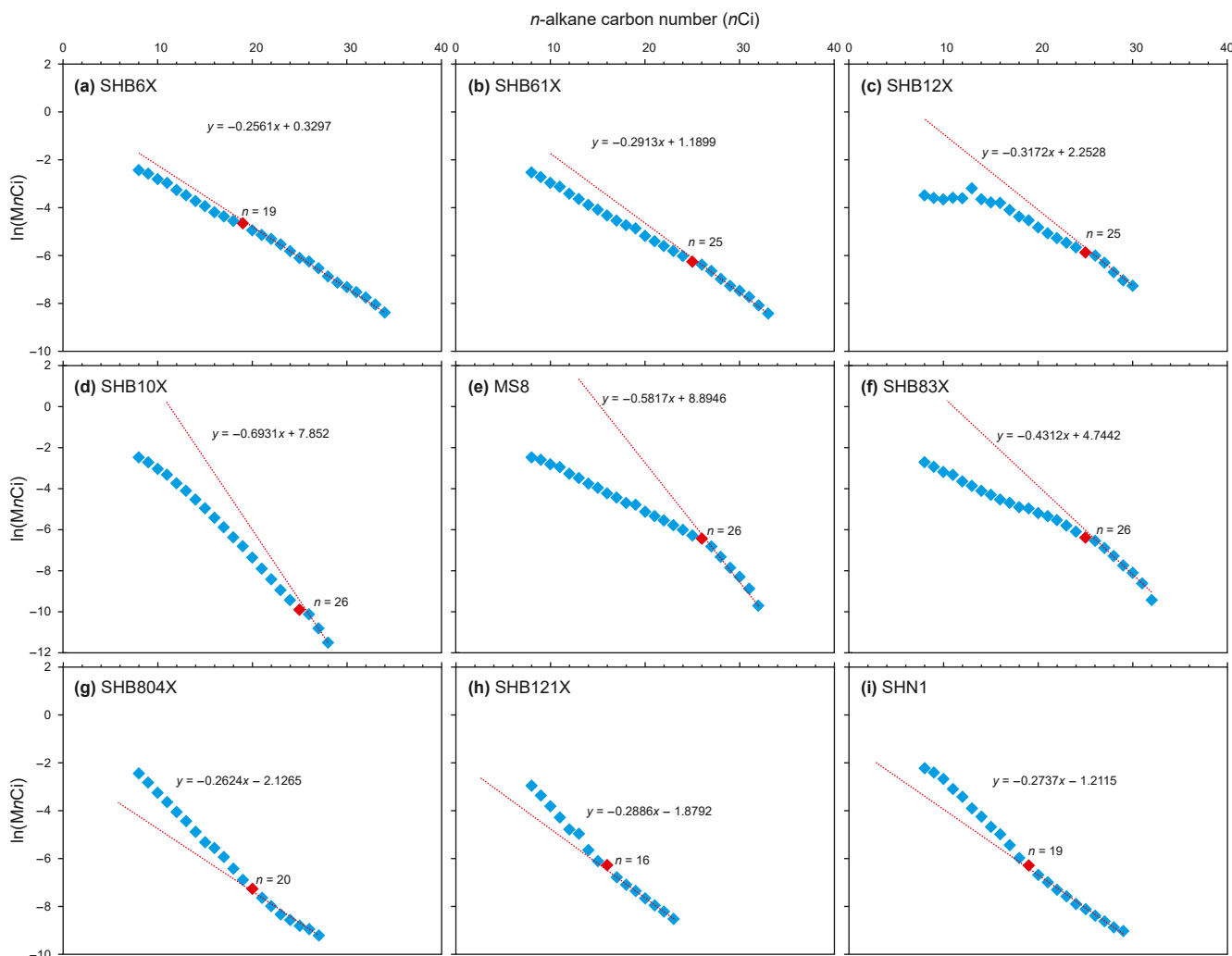


Fig. 14. Variations of the log of mole fraction for the C₈–C₃₅ *n*-alkanes with carbon number ((a)–(i)).

Shunbei Oilfield. Conversely, the Cambrian Awatage and Shayilike formations harbor gypsum-salt layers, creating favorable conditions for TSR (Fig. 1(c)). And analyses of light hydrocarbon parameters, organic sulfur compound contents, and thiadiazonoids suggest the lack of TSR in the Ordovician reservoirs of the Shunbei Oilfield. Evidence of TSR in Ordovician reservoirs primarily originates from potential Cambrian reservoirs, potentially migrating into Ordovician reservoirs during late gas filling.

5.3.5. Evaporative fractionation and gas invasion

The continuous injection of natural gas into the ancient reservoir has correspondingly altered the properties and composition of the original oil. Natural gas dissolves, washes, and filters the original oil, leading to the separation of petroleum phases. This process, which carries away the light fraction in the oil and enriches the heavy fraction, is known as evaporation fractionation (Thompson, 1983; Qiao et al., 2024b). The reaggregated light fractions form reservoirs in new traps or ancient reservoirs, enriching the oil light fractions, a process referred to as gas invasion (Meulbroek et al., 1998). Kissin (1987) observed a good linear relationship between the logarithmic value of the molar concentration of *n*-alkanes in oils not subjected to evaporative fractionation and the carbon number after studying 50 oils from different regions. Oil subjected to evaporative fractionation may experience varying degrees of loss

of *n*-alkanes in light fractions (Kissin, 1987). Conversely, gas invasion can result in an increase in the content of *n*-alkanes in the light fractions of oil (Meulbroek et al., 1998).

Most samples in the study area exhibit evaporative fractionation effects based on the logarithmic distribution of *n*-alkanes in oil (Fig. 14(a)–(f)). Only three wells, SHB804X, SHB121X, and SHN1, exhibit gas invasion (Fig. 14(g)–(i)). Moreover, cross-plotting B-F shows abnormal enrichment of cycloalkanes and aromatics in most oils, indicating varying degrees of evaporative fractionation (Fig. 15; Thompson, 1983). Notably, SHB12X and SHB122X display strong evaporative fractionation effects (Fig. 15(b)). Conversely, the three oil samples affected by gas invasion show abnormal enrichment of cycloparaffins and a relative increase in *n*-alkanes (Fig. 15(b)). Evaporative fractionation and gas invasion, caused by late gas filling, alter the phase distribution of the ancient reservoir. This directly influences the present-phase distribution of petroleum reservoirs.

5.4. Natural gas origin and properties

The $\delta^{13}\text{C}_1$ values of natural gas in the study area range from -44.60‰ to -36.80‰ , averaging at -40.80‰ (Table 4). This, combined with $\text{C}_1/(\text{C}_2+\text{C}_3)$ analysis, indicates predominantly thermogenic gas (Fig. 16(a); Milkov and Etiope, 2018). A cross-plot of

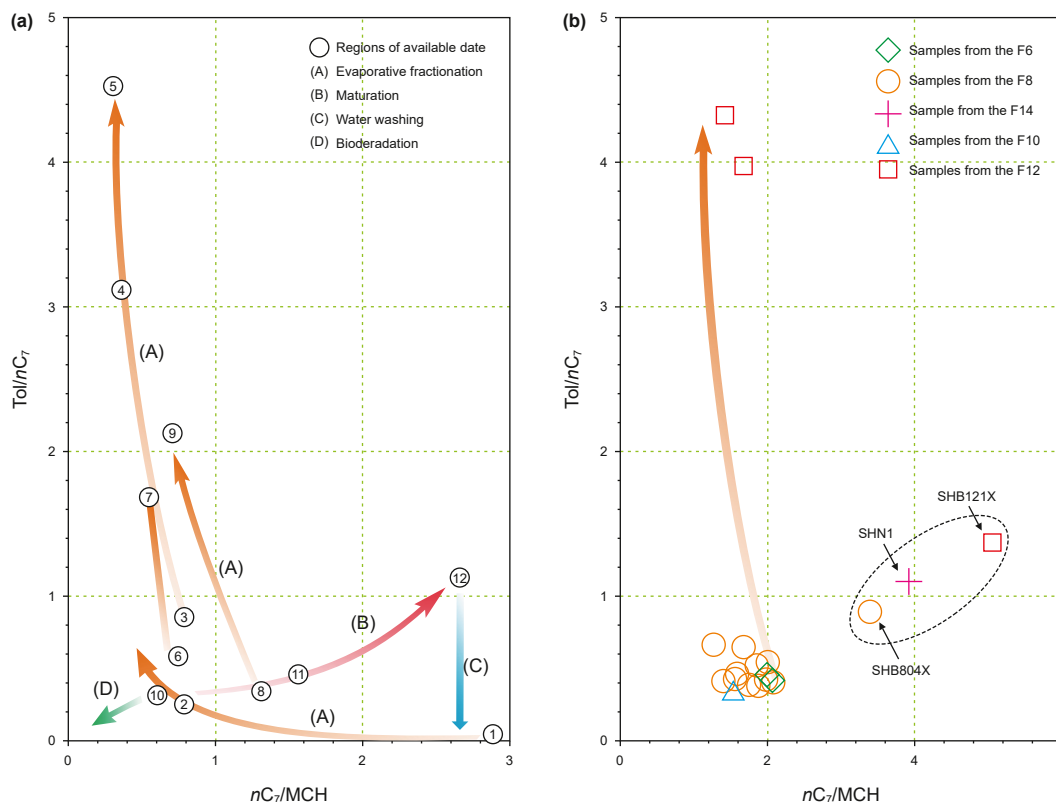


Fig. 15. A cross-plot of Tol/nC₇ versus nC₇/MCH in the light hydrocarbons (refer to Thompson, 1983).

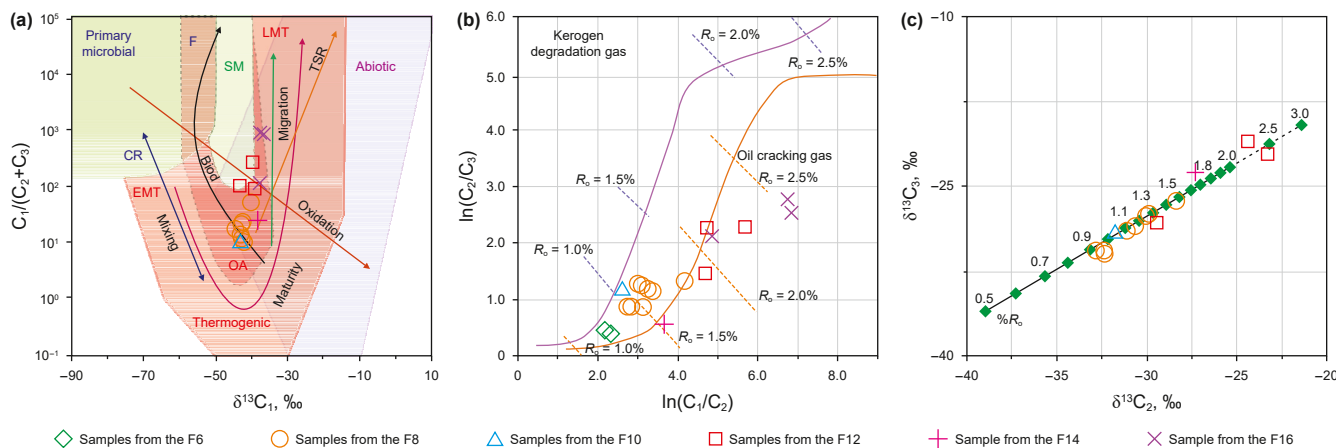


Fig. 16. A cross-plot identifies the origin, type, and equivalent vitrinite reflectance of natural gas. (a) C₁/(C₂+C₃) versus δ¹³C₁ (refer to Milkov and Etiope, 2018); (b) ln(C₂/C₃) versus ln(C₁/C₂) (refer to Xie et al., 2016); (c) δ¹³C₃ versus δ¹³C₂ (refer to Whiticar, 1994).

δ¹³C₁ and C₁/(C₂+C₃) further suggests thermal maturation's influence on the natural gas. Notably, natural gas samples may have migrated in the southern part of the study area. Analyzing ln(C₁/C₂) and ln(C₂/C₃) in a cross-plot reveals a trend from northwest to southeast of kerogen degradation gas transitioning to oil cracking gas (Fig. 16(b); Xie et al., 2016). Most natural gas samples represent a mixture of oil cracking gas and kerogen degradation gas, with only a few wells in the southern region containing typical oil cracking gas (Fig. 16(b)). The cross-plot of δ¹³C₂ and δ¹³C₃ indicates that the gas samples in the study area are mature to overmature, with equivalent vitrinite reflectance ranging from 0.9% to 2.5% (Fig. 16(c); Whiticar, 1994). Additionally, considering the analysis of

evaporative fractionation and gas invasion in the oil samples discussed earlier, late filling in the study area is likely dominated by oil cracking gas. It indicates the presence of ancient oil reservoirs in deep formations.

5.5. Petroleum accumulation

5.5.1. Petroleum filling event and time

Numerous brine and hydrocarbon inclusions were discovered in the Ordovician reservoirs in the study area. Analysis of brine inclusion homogenization temperatures in well SHB84X revealed three distinct peaks at 80–90 °C, 120–130 °C, and 160–170 °C

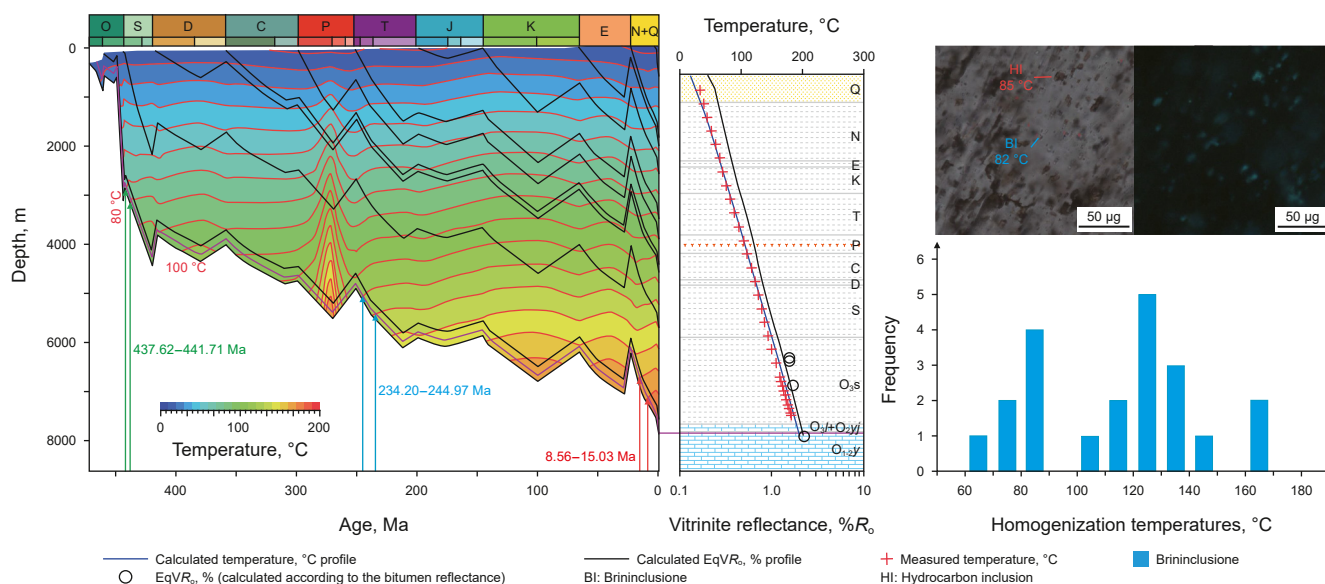


Fig. 17. The burial-thermal history and characters of fluid inclusions in the representative condensate reservoirs in the well SHB84X.

(Fig. 17). This suggests multiple stages of petroleum filling and accumulation in the area.

Analysis of the burial-thermal history and brine inclusion homogenization temperature of well SHB84X determined the petroleum filling periods of the Ordovician reservoir. Three main periods of petroleum filling were identified: late Caledonian (441.71–437.62 Ma), Indosinian (244.97–234.20 Ma), and Himalayan (15.03–8.56 Ma) (Fig. 17).

Previous studies extensively report multi-stage petroleum filling events in this area (Lu et al., 2020; Liu et al., 2021; Li et al., 2022). Most studies identify three periods of petroleum filling events in this area (Fig. 18). The Late Caledonian period (459.88–409.86 Ma) and Hercynian-Indochinese period (275.94–219.77 Ma) were primarily filled with oil, while the Himalayan period (41.90 Ma–2.85 Ma) was dominated by natural gas (Fig. 18). In the northern part of the Shunbei Oilfield, only Late Caledonian and Hercyn-Indosinian oil fills were present due to the thermal evolution of source rocks (Fig. 18; Qiao et al., 2024a). In addition, the Re-Os dating results (399.00 ± 12.00 Ma) and in-situ calcite U-Pb dating results (478.00–384.60 Ma) from previous research on the Tarim Basin support the argument for these two periods of oil filling in the study area, along with illite K-Ar dating results from the reservoir (296.00–204.00 Ma) (Fig. 18; Zhang et al., 2011; Li et al., 2023; Cong et al., 2024; Yuan et al., 2024). The subtle differences between the two results are primarily influenced by regional geological variations, fault properties, and local thermal anomalies (Fig. 18; Yuan et al., 2024; Qiao et al., 2024a).

5.5.2. Petroleum accumulation process and differences

Considering the study of natural gas properties, various secondary alteration affecting oil (e.g., biodegradation, thermal alteration, TSR, evaporative fractionation, and gas invasion), and petroleum filling periods and times, the petroleum accumulation process in the study area was reconstructed.

In the late Caledonian period (478.00–384.60 Ma), the first oil filling event occurred in the Ordovician reservoir of the Shunbei Oilfield (Fig. 19). At this time, the reservoir temperature is less than 80 °C, providing favorable conditions for biodegradation (Fig. 19, I). The detection of 25-norhopane in the oil further confirmed early-stage biodegradation (Fig. 5). Subsequently, during the Permian

Tarim Large Igneous Province (300.00–259.00 Ma), local thermal anomalies resulted in the initially accumulated oil being degraded (Fig. 19, II). These transient thermal anomaly events (e.g., magma intrusion and hydrothermal), characterized by rapid heating rates, can severely damage biomarkers (Figs. 12 and 19, II; Qiao et al., 2024a, 2024c). Therefore, although the current reservoir temperature in F12 is generally higher than 190 °C, biomarker preservation is comparatively better than in other fault zones (Figs. 4 and 19). It is inferred that the biomarker reliability extends to at least 190 °C for oil unaffected by thermal alteration. Seismic profiles mainly indicate evidence of this magmatic intrusion through differences in strong wave impedance between intrusive bodies and surrounding rocks (Fig. 12). Following the cessation of magmatic activity, formation temperatures quickly normalized. Subsequently, during the Hercynian-Indosinian period (296.00–204.00 Ma), a second period of oil from deeper basin regions was filled along the fault (Fig. 19). Biomarker analysis revealed that thermally altered oil did not contain second-period biomarkers. This indicates that oil filled in the Hercynian-Indosinian period mainly originated from deeper reservoirs and was also affected by thermal anomalies. At this time, the formation temperature of the gypsum-salt layer of the Cambrian reaches the threshold of TSR (>120 °C) (Qiao et al., 2024c). The oil begins to be affected by TSR through the interaction of formation water and the gypsum-salt layer (Cai et al., 2022). However, due to variations in the thickness of the gypsum-salt layer, there are significant differences in the degree of TSR affecting the oil. During the Himalayan period (41.90–2.85 Ma), oil-cracking gas from deeper reservoirs began to migrate into shallower reservoirs. During this time, natural gas transported a significant proportion of 2-MH+2,3-DMP and thiadimondoids from Cambrian to Ordovician reservoirs (Fig. 19, IV). Evaporative fractionation and gas washing, induced by natural gas filling, played a major role in shaping the current distribution of petroleum phases. This process is also the primary reason why some condensate is still in the initial stage of cracking.

6. Conclusion

The petroleum accumulation in Ordovician reservoirs in the Shunbei Oilfield is complex due to their diverse properties and

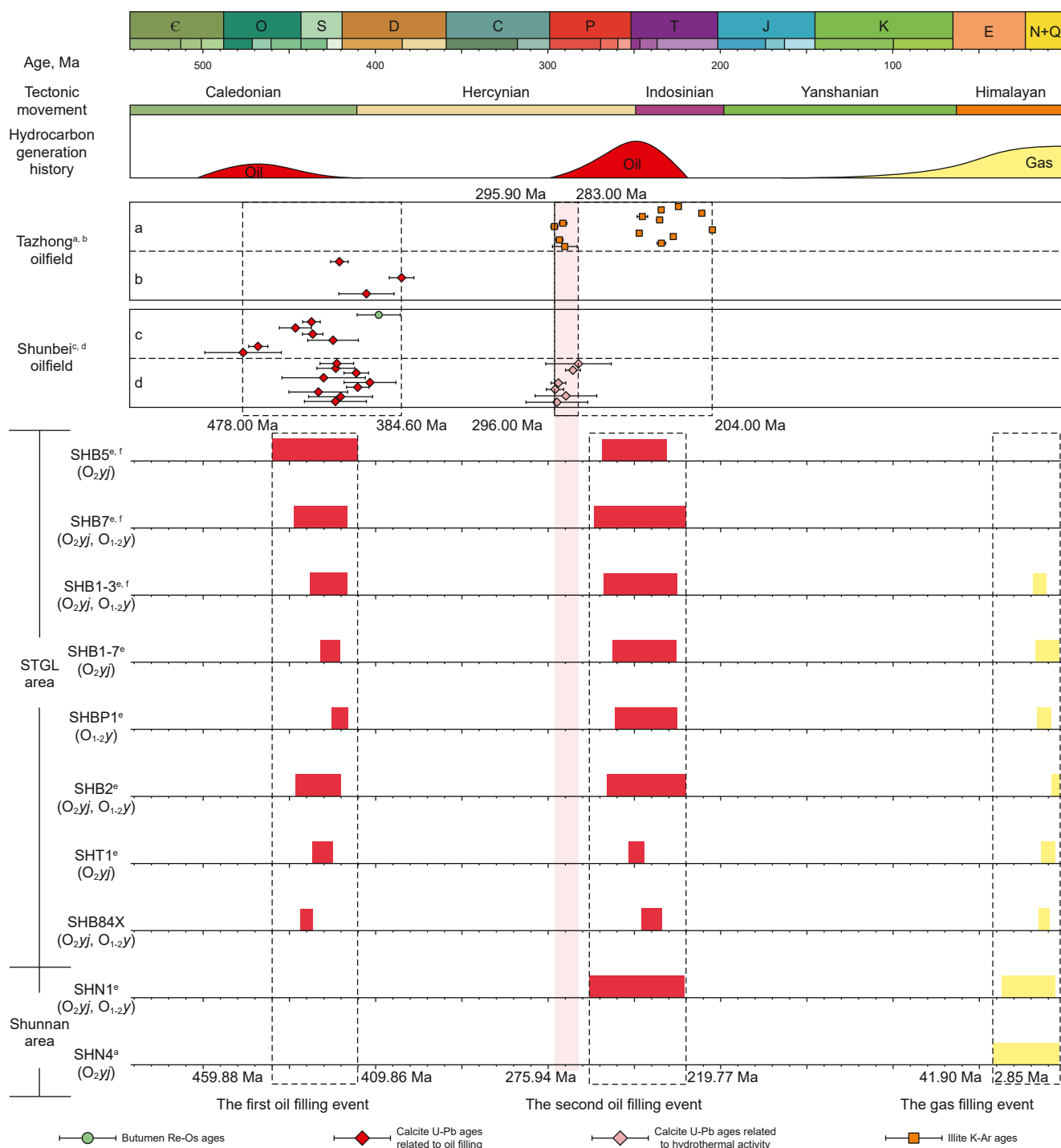


Fig. 18. Schematic diagram of the chronology of hydrocarbon charging in the Cambrian-Ordovician marine carbonate reservoirs in the Shunbei and Tazhong Oilfields. The red square represents oil charging, and the yellow square represents gas charging. (Location of well is shown in Fig. 1(b)). ^a Zhang et al. (2011); ^b Yuan et al. (2024); ^c Cong et al. (2024); ^d Li et al. (2023); ^e Li et al. (2022); ^f Lu et al. (2020).

geochemistry. Through an investigation into the geochemistry and geology of Ordovician petroleum in the Shunbei Oilfield, the following conclusions emerge:

The Ordovician oil in the study area has reached high maturity. A comprehensive analysis reveals three main periods of petroleum filling in the Shunbei area. The Late Caledonian period (478.00–384.60 Ma) and Hercynian Indochinese period (296.00–204.00 Ma) were dominated by oil filling, whereas the

Himalayan period (41.90–2.85 Ma) was characterized by natural gas filling. The oil has undergone biodegradation, thermal alteration, mixing, evaporative fractionation, and gas invasion. Evaporative fractionation and gas invasion significantly influence the present distribution of petroleum phases in the study area.

The rapid increase in formation temperature during Permian magmatic intrusions and hydrothermal activity significantly destroyed oil biomarkers. Biomarker reliability extends to at least

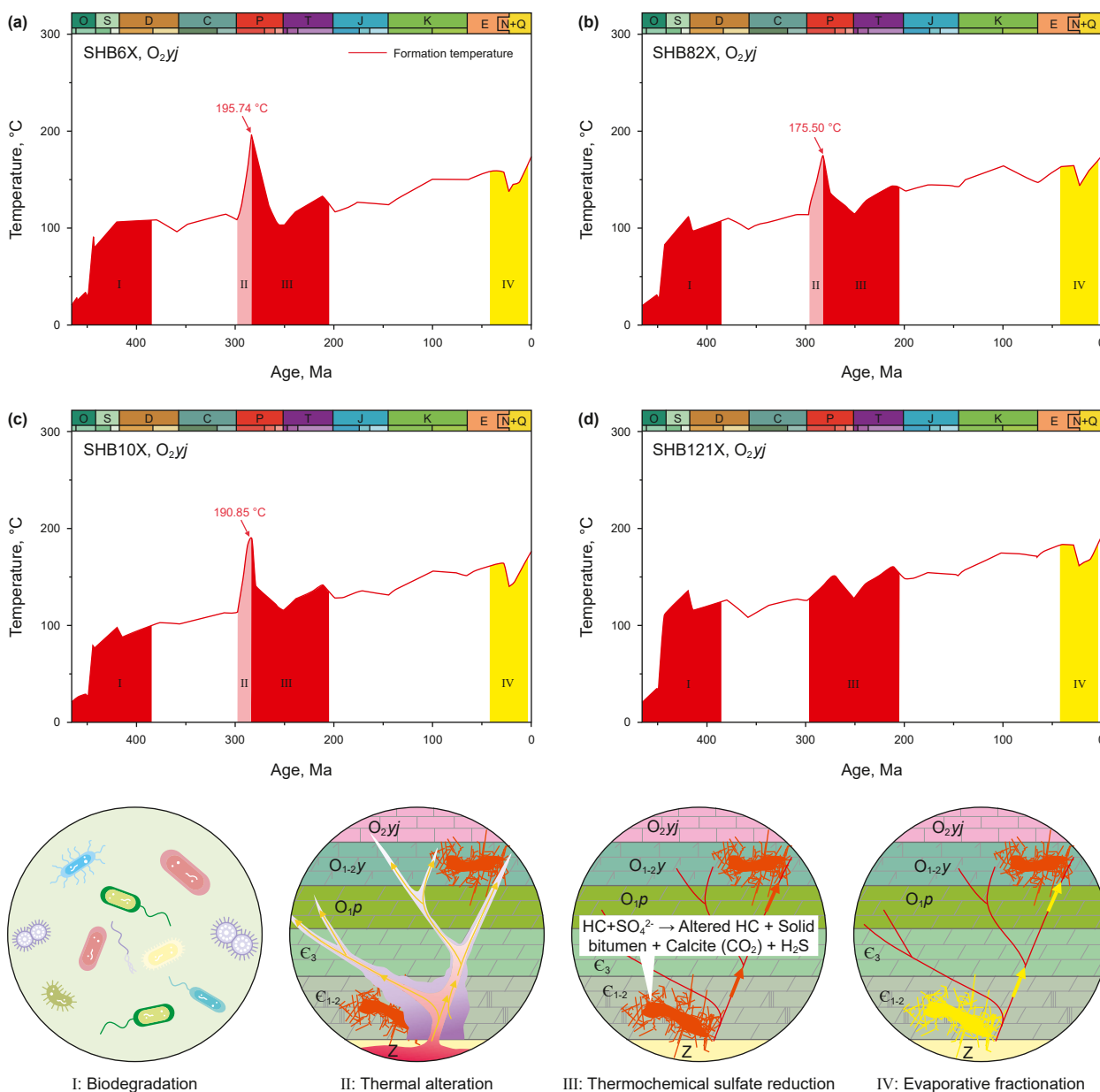


Fig. 19. Reservoir temperature evolution and reservoir-forming model diagram of the Yijianfang Formation (O_{1-2y}), a representative well in Shunbei Oilfield. (a): SHB6X; (b): SHB82X; (c): SHB10X; (d): SHB121X.

190 °C for oil unaffected by thermal alteration.

Indicators of TSR, including light hydrocarbons, aromatic hydrocarbons, and thiadimondoids, suggest that TSR likely occurs in the petroleum reservoirs adjacent to the gypsum-salt layers of the Cambrian system.

The presence of oil cracking gas, evaporation fractionation, and gas invasion further supports the existence of the Cambrian petroleum system in the study area. This finding is crucial for extending petroleum exploration to greater depths. Moreover, it highlights the effective utilization of ultra-deep petroleum geochemistry in reconstructing intricate petroleum accumulation processes.

CRediT authorship contribution statement

Rong-Zhen Qiao: Writing – original draft, Visualization,

Validation, Methodology, Investigation, Conceptualization. **Mei-Jun Li:** Writing – review & editing, Visualization, Supervision. **Dong-Lin Zhang:** Software, Methodology, Investigation, Data curation. **Hong Xiao:** Validation, Supervision, Resources.

Declaration of competing interest

The authors declare that they have no known competing financial interests or personal relationships that could have appeared to influence the work reported in this paper.

Acknowledgements

This work was funded by the National Natural Science Foundations of China (Grant No.42173054). The authors gratefully acknowledge the Northwest Oilfield Company for sample

collection. The author would like to express gratitude to the associate editor, Dr. Jie Hao, and the three anonymous reviewers for their valuable and constructive reviews, which have substantially enhanced the manuscript.

Appendix A. Supplementary data

Supplementary data to this article can be found online at <https://doi.org/10.1016/j.petsci.2025.02.019>.

References

- Bennett, B., Fustic, M., Farrimond, P., Huang, H.P., Larter, S.R., 2006. 25-NHs: formation during biodegradation of petroleum in the subsurface. *Org. Geochem.* 37, 787–797. <https://doi.org/10.1016/j.orggeochem.2006.03.003>.
- Cai, C., Hu, W., Worden, R.H., 2001. Thermochemical sulfate reduction in Cambro-Ordovician carbonates in central tarim. *Mar. Petrol. Geol.* 18, 729–741. [https://doi.org/10.1016/S0264-8172\(01\)00028-9](https://doi.org/10.1016/S0264-8172(01)00028-9).
- Cai, C., Zhang, C., Worden, R.H., Wang, T., Li, H., Jiang, L., Huang, S., Zhang, B., 2015. Application of sulfur and carbon isotopes to oil–source rock correlation: a case study from the Tazhong area, Tarim Basin, China. *Org. Geochem.* 83–84, 140–152. <https://doi.org/10.1016/j.orggeochem.2015.03.012>.
- Cai, C., Amrani, A., Worden, R.H., Xiao, Q., Wang, T., Gvirtzman, Z., Li, H., Said-Ahmad, W., Jia, L., 2016a. Sulfur isotopic compositions of individual organo-sulfur compounds and their genetic links in the Lower Paleozoic petroleum pools of the Tarim Basin, NW China. *Geochem. Cosmochim. Acta* 182, 88–108. <https://doi.org/10.1016/j.gca.2016.02.036>.
- Cai, C., Xiao, Q., Fang, C., Wang, T., He, W., Li, H., 2016b. The effect of thermochemical sulfate reduction on formation and isomerization of thiadiazonoids and diamondoids in the Lower Paleozoic petroleum pools of the Tarim Basin, NW China. *Org. Geochem.* 101, 49–62. <https://doi.org/10.1016/j.orggeochem.2016.08.006>.
- Cai, C., Li, H., Li, K., Wang, D., 2022. Thermochemical sulfate reduction in sedimentary basins and beyond: a review. *Chem. Geol.* 607, 121018. <https://doi.org/10.1016/j.chemgeo.2022.121018>.
- Cao, Z., Ma, A., Xu, Q., Pan, Q., Shang, K., Feng, F., Liu, Y., 2024. Geochemical characteristics and exploration significance of ultra-deep Sinian oil and gas from Well Tashen 5, Tarim Basin, NW China. *Energy Geosci* 5 (1), 100217. <https://doi.org/10.1016/j.engeos.2023.100217>.
- Chen, J., Fu, J., Sheng, G., Liu, D., Zhang, J., 1996. Diamondoid hydrocarbon ratios: novel maturity indices for highly mature crude oil. *Org. Geochem.* 25, 179–190. [https://doi.org/10.1016/S0146-6380\(96\)00125-8](https://doi.org/10.1016/S0146-6380(96)00125-8).
- Chen, Z., Chai, Z., Cheng, B., Liu, H., Cao, Y., Cao, Z., Qu, J., 2021. Geochemistry of high-maturity crude oil and gas from deep reservoirs and their geological significance: a case study on Shuntuoguole low uplift, Tarim Basin, western China. *AAPG Bull.* 105 (1), 65–107. <https://doi.org/10.1306/07072019015>.
- Cong, F., Tian, J., Hao, F., Wang, Q., Kylander-Clark, A.R.C., Cao, Z., 2024. In-situ calcite U-Pb ages and absolute timing of oil charge events: a case study of ultra-deep carbonate reservoirs in the Shunbei oilfield, Tarim basin, Northwest China. *J. Asian Earth Sci.* 259, 105904. <https://doi.org/10.1016/j.jseas.2023.105904>.
- Dahl, J.E., Moldowan, J.M., Peters, K.E., Claypool, G.E., Rooney, M.A., Michael, G.E., Mello, M.R., Kohnen, M.L., 1999. Diamondoid hydrocarbons as indicators of natural oil cracking. *Nature* 399, 54–57. <https://doi.org/10.1038/19953>.
- Deng, H., Zhang, H., Zhang, Y., Chen, N., Mo, T., Cheng, B., Liao, Z., 2023. Genetic identification of light oils and condensates using δD indices of C_7 hydrocarbons: a case study in the Tarim Basin, NW China. *Int. J. Coal Geol.* 279, 104372. <https://doi.org/10.1016/j.coal.2023.104372>.
- Dong, S., Chen, D., Qing, H., Zhou, X., Wang, D., Guo, Z., Jiang, M., Qian, Y., 2013. Hydrothermal alteration of dolostones in the Lower Ordovician, Tarim Basin, NW China: multiple constraints from petrology, isotope geochemistry and fluid inclusion microthermometry. *Mar. Petrol. Geol.* 46, 270–286. <https://doi.org/10.1016/j.marpetgeo.2013.06.013>.
- Du, J., Li, X., Bao, H., Xu, W., Wang, Y., Huang, J., Wang, H., Wangyan, R., Wang, J., 2019. Geological conditions of natural gas accumulation and new exploration areas in the Mesoproterozoic to Lower Paleozoic of Ordos Basin, NW China. *Petrol. Explor. Dev.* 46 (5), 866–882. [https://doi.org/10.1016/S1876-3804\(19\)60246-6](https://doi.org/10.1016/S1876-3804(19)60246-6).
- Fang, X., Deng, B., Geng, A., Liu, S., Wang, P., Xiao, L., Li, Y., Cheng, B., Jiang, W., Wu, L., 2024. Geochemical properties, mechanism of formation, and source of solid bitumen in the Ediacaran Dengying Formation from the central to northern Sichuan Basin, China. *Mar. Petrol. Geol.* 159, 106573. <https://doi.org/10.1016/j.marpetgeo.2023.106573>.
- Gvirtzman, Z., Said-Ahmad, W., Ellis, G.S., Hill, R.J., Moldowan, J.M., Wei, Z., Amrani, A., 2015. Compound-specific sulfur isotope analysis of thiadiazonoids of oils from the Smackover Formation, USA. *Geochem. Cosmochim. Acta* 167, 144–161. <https://doi.org/10.1016/j.gca.2015.07.008>.
- He, D., Jia, C., Zhao, W., Xu, F., Luo, X., Liu, W., Tang, Y., Gao, S., Zheng, X., Li, D., Zheng, N., 2023. Research progress and key issues of ultra-deep oil and gas exploration in China. *Petrol. Explor. Dev.* 50 (6), 1333–1344. [https://doi.org/10.1016/S1876-3804\(24\)60470-2](https://doi.org/10.1016/S1876-3804(24)60470-2).
- He, J., Ding, W., Huang, W., Cao, Z., Chen, E., Dai, P., Zhang, Y., 2019. Petrological, geochemical, and hydrothermal characteristics of Ordovician cherts in the southeastern Tarim Basin, NW China, and constraints on the origin of cherts and Permian tectonic evolution. *J. Asian Earth Sci.* 170, 294–315. <https://doi.org/10.1016/j.jseas.2018.10.030>.
- Hu, T., Ge, B., Zhang, Y., Liu, B., 1990. The development and application of fingerprint parameters for hydrocarbons absorbed by source rocks and light hydrocarbons in natural gas. *Petrol. Geol. Exp.* 12, 375–393 (in Chinese).
- Hunt, J.M., 1984. Generation and migration of light hydrocarbons. *Science* 226, 1265–1270. <https://doi.org/10.1126/science.226.4680.1265>.
- Kissin, Y.V., 1987. Catagenesis and composition of petroleum: origin of n-alkanes and isoalkanes in petroleum crudes. *Geochem. Cosmochim. Acta* 51, 2445–2457. [https://doi.org/10.1016/0016-7037\(87\)90296-1](https://doi.org/10.1016/0016-7037(87)90296-1).
- Kontorovich, A.E., Kashirtsev, V.A., Melenevskii, V.H., Timoshina, I.D., 2005. Composition of biomarker-hydrocarbons in genetic families of Precambrian and Cambrian oils of the Siberian platform. *Dokl. Earth Sci.* 403, 715–718. <https://doi.org/10.1016/j.cageo.2004.12.001>.
- Krouse, H.R., Viau, C.A., Eliuk, L.S., Ueda, A., Halas, S., 1988. Chemical and isotopic evidence of thermochemical sulphate reduction by light hydrocarbon gases in deep carbonate reservoirs. *Nature* 333, 415–419. <https://doi.org/10.1038/333415a0>.
- Li, D., Chang, J., Qiu, N., Wang, J., Zhang, M., Wu, X., Han, J., Li, H., Ma, A., 2022. The thermal history in sedimentary basins: a case study of the central Tarim Basin, Western China. *J. Asian Earth Sci.* 229, 105149. <https://doi.org/10.1016/j.jseas.2022.105149>.
- Li, H., Cai, C., Jia, L., Xu, C., Zhang, K., 2017. The effect of water chemistry on thermochemical sulfate reduction: a case study from the Ordovician in the Tazhong area, northwest China. *Geofluids* 34, 1–14. <https://doi.org/10.1155/2017/6351382>.
- Li, H., Gao, J., Cao, Z., Zhu, X., Guo, X., Zeng, S., 2023. Spatial-temporal distribution of fluid activities and its significance for hydrocarbon accumulation in the strike-slip fault zones, Shuntuoguole low-uplift, Tarim Basin. *Earth Sci. Front.* 30 (6), 316–328. <https://doi.org/10.13745/j.esf.sc.2023.2.36> (in Chinese).
- Liu, Y., Dong, S., Zhao, C., 2021. Thermal evolution and the maturation of the deeply buried lower Paleozoic source rocks in the Tarim Basin, northwest China. *Arabian J. Geosci.* 14, 1238. <https://doi.org/10.1007/s12517-021-07562-w>.
- Losh, S., Cathles, L., Meulbroek, P., 2002. Gas washing of oil along a regional transect, offshore Louisiana. *Org. Geochem.* 33 (6), 655–663. [https://doi.org/10.1016/S0146-6380\(02\)00025-6](https://doi.org/10.1016/S0146-6380(02)00025-6).
- Lu, Z., Li, Y., Ye, N., Zhang, S., Lu, C., Li, W., Cheng, Z., Ding, X., Zhu, B., Huang, B., Chen, S., 2020. Fluid inclusions record hydrocarbon charge history in the Shunbei Area, Tarim Basin, NW China. *Geofluids* 2020, 1–15. <https://doi.org/10.1155/2020/8847247>.
- Ma, Y., Cai, X., Yun, L., Li, Z., Li, H., Deng, S., Zhao, P., 2022. Peirong Practice and theoretical and technical progress in exploration and development of Shunbei ultra-deep carbonate oil and gas field, Tarim Basin, NW China. *Petrol. Explor. Dev.* 49 (1), 1–20. [https://doi.org/10.1016/S1876-3804\(22\)60001-6](https://doi.org/10.1016/S1876-3804(22)60001-6).
- Mackenzie, A.S., Patience, R.L., Maxwell, J.R., Vandenbroucke, M., Durand, B., 1980. Molecular parameters of maturation in the Toarcian shales, Paris Basin, France. I. Changes in the configurations of acyclic isoprenoid alkanes, steranes and triterpanes. *Geochem. Cosmochim. Acta* 44 (11), 1709–1721. [https://doi.org/10.1016/0016-7037\(80\)90222-7](https://doi.org/10.1016/0016-7037(80)90222-7).
- Mango, F.D., 1997. The light hydrocarbons in petroleum: a critical review. *Org. Geochem.* 26 (7–8), 417–440. [https://doi.org/10.1016/S0146-6380\(97\)00031-4](https://doi.org/10.1016/S0146-6380(97)00031-4).
- Meulbroek, P., Cathles, L., Whelan, J., 1998. Phase fractionation at south edge island block 330. *Org. Geochem.* 29, 223–239. [https://doi.org/10.1016/S0146-6380\(98\)00180-6](https://doi.org/10.1016/S0146-6380(98)00180-6).
- Milkov, A.V., Etiope, G., 2018. Revised genetic diagrams for natural gases based on a global dataset of >20,000 samples. *Org. Geochem.* 125, 109–120. <https://doi.org/10.1016/j.orggeochem.2018.09.002>.
- Moldowan, J.M., Dahl, J., Zinniker, D., Barbanti, S.M., 2015. Underutilized advanced geochemical technologies for oil and gas exploration and production-1. The diamondoids. *J. Petrol. Sci. Eng.* 126, 87–96. <https://doi.org/10.1016/j.petrol.2014.11.010>.
- Moldowan, J.M., McCaffrey, M.A., 1995. A novel microbial hydrocarbon degradation pathway revealed by hopane demethylation in a petroleum reservoir. *Geochem. Cosmochim. Acta* 59, 1891–1894. [https://doi.org/10.1016/0016-7037\(95\)00072-8](https://doi.org/10.1016/0016-7037(95)00072-8).
- Ning, F., Yun, J., Zhang, Z., Li, P., 2022. Deformation patterns and hydrocarbon potential related to intracratonic strike-slip fault systems in the east of Central Uplift Belt in the Tarim Basin. *Energy Geosci* 3 (1), 63–72. <https://doi.org/10.1016/j.engeos.2021.10.008>.
- Othman, R., Arouri, K.R., Ward, C.R., McKirdy, D.M., 2001. Oil generation by igneous intrusions in the northern Gunnedah Basin, Australia. *Org. Geochem.* 32 (10), 1219–1232. [https://doi.org/10.1016/S0146-6380\(01\)00089-4](https://doi.org/10.1016/S0146-6380(01)00089-4).
- Peng, Y., Cai, C., Fang, C., Wu, L., Liu, D., Sun, P., Liu, D., 2022. Diamondoids and thiadiazonoids generated from hydrothermal pyrolysis of crude oil and TSR experiments. *Sci. Rep.* 12, 196. <https://doi.org/10.1038/s41598-021-04270-z>.
- Peters, K.E., Moldowan, J.M., 1993. *The Biomarker Guide; Interpreting Molecular Fossils in Petroleum and Ancient Sediments*. Prentice Hall, Englewood Cliffs, NJ.
- Peters, K.E., Walters, C.C., Moldowan, J.M., 2005. *The Biomarker Guide*. Cambridge University Press, Cambridge.
- Qi, Y., Sun, P., Cai, C., Wang, D., Peng, Y., 2022. Phase fractionation controlling regional distribution of diamondoids: a case study from the Halahatang oil field, Tarim Basin, China. *Mar. Petrol. Geol.* 140, 105674. <https://doi.org/10.1016/j.marpetgeo.2022.105674>.

- Qiao, R., Chen, Z., 2022. Petroleum phase evolution at high temperature: a combined study of oil cracking experiment and deep oil in Dongying Depression, eastern China. *Fuel* 326, 124978. <https://doi.org/10.1016/j.fuel.2022.124978>.
- Qiao, R., Chen, Z., Li, C., Wang, D., Gao, Y., Zhao, L., Li, Y., Liu, J., 2022. Geochemistry and accumulation of petroleum in deep lacustrine reservoirs: a case study of Dongying Depression, Bohai Bay Basin. *J. Petrol. Sci. Eng.* 213, 110433. <https://doi.org/10.1016/j.petrol.2022.110433>.
- Qiao, R., Li, M., Zhang, D., Xiao, H., 2024a. Geochemistry and accumulation of the ultra-deep Ordovician oils in the Shunbei oilfield, Tarim Basin: coupling of reservoir secondary processes and filling events. *Mar. Petrol. Geol.* 167, 106959. <https://doi.org/10.1016/j.marpetgeo.2024.106959>.
- Qiao, R., Li, M., Zhang, D., Chen, Z., Xiao, H., 2024b. Evaporative fractionation as the important formation mechanism of light oil reservoirs in the dongying depression, NE China. *Energies* 17, 3734. <https://doi.org/10.3390/en17153734>.
- Qiao, R., Li, M., Zhang, D., Xiao, H., 2024c. Distribution and origin of higher diamondoids in the ultra-deep Paleozoic condensates of the Shunbei oilfield in the Tarim Basin, NW China. *Org. Geochem.* 197, 104883. <https://doi.org/10.1016/j.orggeochem.2024.104883>.
- Qiao, R., Li, M., Zhang, D., Xiao, H., Wang, W., 2025. Polycyclic aromatic compounds in crude oil as proxies for Permian Tarim large igneous province activities. *Geosci. Front.* 16 (2), 102000. <https://doi.org/10.1016/j.gsf.2024.102000>.
- Schulz, L.K., Wilhelms, A., Rein, E., Steen, A.S., 2001. Application of diamondoids to distinguish source rock facies. *Org. Geochem.* 32, 365–375. [https://doi.org/10.1016/S0146-6380\(01\)00003-1](https://doi.org/10.1016/S0146-6380(01)00003-1).
- Shanmugam, G., 1985. Significance of coniferous rain forests and related organic matter in generating commercial quantities of oil, gippsland basin, Australia. *AAPG Bull.* 69 (8), 1241–1254. <https://doi.org/10.1306/AD462BC3-16F7-11D7-8645000102C1865D>.
- Simoneit, B., Brenner, S., Peters, K., Kaplan, I.R., 1978. Thermal alteration of Cretaceous black shale by basaltic intrusions in the Eastern Atlantic. *Nature* 273, 501–504. <https://doi.org/10.1038/273501a0>.
- Song, D., Zhang, C., Li, S., Wang, T., Li, M., 2017. Elevated mango's K1 values resulting from thermochemical sulfate reduction within the Tazhong oils, Tarim Basin. *Energy Fuels* 31, 1250–1258. <https://doi.org/10.1021/acs.energyfuels.6b02503>.
- Sun, Y., Chen, Z., Xu, S., Cai, P., 2005. Stable carbon and hydrogen isotopic fractionation of individual n-alkanes accompanying biodegradation: evidence from a group of progressively biodegraded oils. *Org. Geochem.* 36, 225–238. <https://doi.org/10.1016/j.orggeochem.2004.09.002>.
- Thompson, K.F.M., 1983. Classification and thermal history of petroleum based on light hydrocarbons. *Geochem. Cosmochim. Acta* 47 (2), 303–316. [https://doi.org/10.1016/0016-7037\(83\)90143-6](https://doi.org/10.1016/0016-7037(83)90143-6).
- Walters, C.C., Isaksen, G.H., Peters, K.E., 2003. Applications of light hydrocarbon molecular and isotopic compositions in oil and gas exploration. In: Hsu, C.S. (Ed.), *Analytical Advances for Hydrocarbon Research. Modern Analytical Chemistry*. Springer, Boston, MA.
- Wang, D., Cai, C., Yun, L., Liu, J., Sun, P., Jiang, Z., Peng, Y., Zhang, H., Wei, T., Pei, B., 2023. Controls on petroleum stability in deep and hot reservoirs: a case study from the Tarim Basin. *Mar. Petrol. Geol.* 147, 106014. <https://doi.org/10.1016/j.marpetgeo.2022.106014>.
- Wang, Q., Hao, F., Cao, Z., Tian, J., Cong, F., 2021. Geochemistry and origin of the ultra-deep Ordovician oils in the Shunbei field, Tarim Basin, China: implications on alteration and mixing. *Mar. Petrol. Geol.* 123, 104725. <https://doi.org/10.1016/j.marpetgeo.2020.104725>.
- Whiticar, M.J., 1994. Correlation of natural gases with their sources. In: Magoon, L.B., Dow, W.G. (Eds.), *The Petroleum System—From Source to Trap*, vol. 60. AAPG Memoir, pp. 261–283.
- Wilhelms, A., Larter, S., 2004. Shaken but not always stirred. Impact of petroleum charge mixing on reservoir geochemistry. *Geological Society* 237 (1), 27–35. <https://doi.org/10.1144/GSL.SP.2004.237.01.03>.
- Xie, Z., Li, Z., Wei, G., Li, J., Wang, D., Wang, Z., Dong, C., 2016. Experimental research on the potential of sapropelic kerogen degradation gas and discrimination of oil cracking gas. *Nat. Gas Geosci.* 1 (6), 471–479. <https://doi.org/10.1016/j.jnggs.2016.11.010>.
- Xu, H., Liu, Q., Zhu, D., Peng, W., Meng, Q., Wang, J., Shi, J., Jin, Z., 2022. Molecular evidence reveals the presence of hydrothermal effect on ultra-deep-preserved organic compounds. *Chem. Geol.* 608, 121045. <https://doi.org/10.1016/j.chemgeo.2022.121045>.
- Xu, K., Yu, B., Gong, H., Ruan, Z., Pang, Y., Ren, Y., 2015. Carbonate reservoirs modified by magmatic intrusions in the Bachu area, Tarim Basin, NW China. *Geosci. Front.* 6 (5), 779–790. <https://doi.org/10.1016/j.gsf.2015.02.002>.
- Yao, G., Wu, X., Sun, Z., Yu, C., Ge, Y., Yang, X., Wen, L., Ni, C., Fu, X., Zhang, J., 2018. Status and prospects of exploration and exploitation key technologies of the deep petroleum resources in onshore China. *Nat. Gas Geosci.* 3 (1), 25–35. <https://doi.org/10.1016/j.jnggs.2018.03.002>.
- Yuan, F., Yang, X., Zhang, K., Tian, J., Hao, F., Kylander-Clark, A.R.C., Cong, F., Wang, X., 2024. Multiple geochronological evidences revealing oil charging and redistribution processes in the Tazhong-4 Oilfield, Tazhong Uplift (Tarim Basin): implications for quantitative reconstruction of petroleum accumulation history in superimposed basins. *Mar. Petrol. Geol.* 162, 106688. <https://doi.org/10.1016/j.marpetgeo.2023.106688>.
- Zhang, D., Li, M., Qiao, R., Xiao, H., 2024. Applicability and limitation of aromatic maturity parameters in high-maturity oil from ultradeep reservoirs. *Energy & Fuels* 38, 18413–18430. <https://doi.org/10.1021/acs.energyfuels.4c02159>.
- Zhang, S., Su, J., Wang, X., Ma, S., 2022. Sedimentary environments of cambrian–ordovician source rocks and ultra-deep petroleum accumulation in the Tarim Basin. *Acta Geol. Sin.* 96 (4), 1259–1276. <https://doi.org/10.1111/1755-6724.14982>.
- Zhang, Y., Zwingmann, H., Liu, K., Todd, A., Luo, X., 2011. Hydrocarbon charge history of the Silurian bituminous sandstone reservoirs in the Tazhong uplift, Tarim Basin, China. *AAPG Bull.* 95 (3), 395–412. <https://doi.org/10.1306/08241009208>.
- Zhang, Z., Zhu, G., Han, J., Sun, C., Huang, C., Li, J., Zhao, K., 2022. Genesis and preservation of the giant ultradeep Hadexun petroleum accumulation in the Tarim Basin, China. *J. Petrol. Sci. Eng.* 208, 109249. <https://doi.org/10.1016/j.petrol.2021.109249>.
- Zhu, G., Zhang, Z., Zhou, X., Li, T., Han, J., Sun, C., 2019. The complexity, secondary geochemical process, genetic mechanism and distribution prediction of deep marine oil and gas in the Tarim Basin, China. *Earth Sci. Rev.* 198, 102930. <https://doi.org/10.1016/j.earscirev.2019.102930>.
- Zhu, G., Zhao, K., Li, T., Zhang, Z., Zhao, K., Zhang, K., Chen, W., Ya, H., Wang, P., 2020. Distribution and geodynamic setting of the late neoproterozoic–early cambrian hydrocarbon source rocks in the south China and tarim blocks. *J. Asian Earth Sci.* 201, 104504. <https://doi.org/10.1016/j.jseas.2020.104504>.
- Zhu, G., Milkov, A.V., Li, J., Xue, N., Chen, Y., Hu, J., Li, T., Zhang, Z., Chen, Z., 2021. Deepest oil in Asia: characteristics of petroleum system in the Tarim basin, China. *J. Petrol. Sci. Eng.* 199, 108246. <https://doi.org/10.1016/j.petrol.2020.108246>.
- Zhu, G., Zhang, K., 2022. Did the eruption of the Tarim LIP control the formation of Paleozoic hydrocarbon reservoirs in the Tarim basin, China? *Gondwana Res.* 101, 224–232. <https://doi.org/10.1016/j.gr.2021.08.007>.